学位論文

Measurability of virtual photon polarization due to intense
magnetic field generated in Pb-Pb collisions at
$$\sqrt{s_{\mathrm{NN}}} = 5.36 \text{ TeV}$$

(核子対あたり重心系エネルギー 5.36 TeV 鉛鉛原子核衝突
における強磁場起因仮想光子偏光の測定可能性)

2025 年

広島大学大学院　先進理工系科学研究科
先進理工系科学専攻　物理学プログラム
クォーク物理学研究室

木村　健斗

Ph.D Thesis

Measurability of virtual photon polarization due to intense
magnetic field generated in Pb-Pb collisions at
$$\sqrt{s_{\mathrm{NN}}} = 5.36 \text{ TeV}$$

Graduate School of Advanced Science and Engineering in Hiroshima University
Physics program
Quark Physics Laboratory

Kento Kimura

目次

主論文

Abstract

Research on the quark–gluon plasma (QGP) in high-energy heavy-ion collisions has spanned over four decades, advancing our understanding of Quantum Chromodynamics (QCD). Recently, attention has shifted to the intense electromagnetic fields generated during these collisions. These fields may exceed the Schwinger limit, potentially reaching strengths of up to 10^{15} T at LHC energies. Such extreme conditions not only present a unique testbed for nonlinear QED phenomena but may also significantly influence the QCD matter formed in the collision.

Although various attempts have been made to observe these intense magnetic fields, direct experimental evidence remains elusive. A promising approach involves virtual photons produced concurrently with the magnetic field at early times. Because virtual photons can decay into lepton pairs without traversing the bulk QCD medium, they offer a direct window onto magnetic-field effects. In particular, the polarization of these photons, reflected in the angular distribution of the resulting lepton pairs, may reveal how strong fields alter electromagnetic processes in heavy-ion collisions.

The main aim of this work is to investigate the polarization of virtual photons under a strong magnetic field and evaluate whether such polarization can be measured in current or future ALICE datasets. Focusing on muon pairs ($\mu^+\mu^-$) detected by the ALICE muon spectrometer, we analyze prompt virtual photons generated at the collision's earliest stages while taking background processes into account. Because Dalitz decays of pions, which often dominate the electron–positron channel, are largely absent in the muon channel, we expect a better signal-to-background ratio.

Our study integrates a realistic time evolution of the magnetic field, modeled with resistive relativistic magnetohydrodynamics (RRMHD). We find that the virtual photon polarization P_{cal} could reach about 0.05 under typical LHC conditions. However, preliminary significance estimates indicate a low detection probability based on the data of Pb-Pb collisions collected in 2011–2012 or 2015–2018. In contrast, future and ongoing runs at $\sqrt{s_{\mathrm{NN}}} = 5.36$ TeV will benefit from higher collision rates and continuous data readout, substantially boosting the available statistics. This improvement raises the prospect of measuring virtual photon polarization as a novel probe of the intense electromagnetic fields in heavy-ion collisions.

Contents

List of Figures

6

1 Introduction

1.1 Quantum Electrodynamics (QED)

Quantum Electrodynamics (QED) is a theory that describes how electrically charged particles, such as electrons, interact with electromagnetic fields. It combines the principles of quantum mechanics, which govern small-scale phenomena, and special relativity, which describes high-speed motion. This unification allows QED to explain the behavior of particles and fields in a way that agrees with experiments to an extraordinary degree of precision.

The central mathematical expression in QED is called the Lagrangian density, which encodes the rules governing the behavior of charged particles and electromagnetic fields. It is given by:

$$
\begin{aligned}
\mathcal{L}_{\text{QED}} &= \sum_f \bar{\psi}_f (i\gamma^\mu D_\mu - m)\psi_f - \frac{1}{4} F_{\mu\nu} F^{\mu\nu} \\
&= \sum_f \bar{\psi}_f (i\gamma^\mu \partial_\mu - m)\psi_f - \sum_f e\bar{\psi}_f \gamma^\mu A_\mu \psi_f - \frac{1}{4} F_{\mu\nu} F^{\mu\nu},
\end{aligned}
\tag{1.1}
$$

where, ψ represents the Dirac spinor field, which describes the charged fermions, like electrons. The term $\bar{\psi}$ is the adjoint spinor, related to ψ through the conjugate and the gamma matrices. The γ^μ matrices are essential for ensuring that the theory is consistent with special relativity. The covariant derivative, $D_\mu = \partial_\mu + ieA_\mu$, describes how charged particles interact with the electromagnetic field, where A_μ is the four-potential of the electromagnetic field and e is the electric charge of the fermion. The field intensity tensor, $F_{\mu\nu} = \partial_\mu A_\nu - \partial_\nu A_\mu$, encodes the electric and magnetic field components in a relativistically invariant form. Finally, m denotes the mass of the fermion.

The Lagrangian can be broken into three distinct parts. The first term, $\bar{\psi}(i\gamma^\mu \partial_\mu - m)\psi$, describes the motion of a free charged fermion with mass m. It consists of two components: the first part, $\bar{\psi} i\gamma^\mu \partial_\mu \psi$, represents the kinetic energy of the fermion, while the second part, $-m\bar{\psi}\psi$, accounts for the rest mass energy of the fermion. The second term, $-e\bar{\psi}\gamma^\mu A_\mu \psi$, represents the interaction between the charged fermion and the electromagnetic field. The coupling constant e determines the intensity of this interaction, while the factor $\gamma^\mu A_\mu$ ensures that the interaction is relativistically formulated. The third term, $-\frac{1}{4} F_{\mu\nu} F^{\mu\nu}$, governs the dynamics of the electromagnetic field itself, describing both the energy density of the electric and magnetic fields and their propagation through space-time.

This Lagrangian provides a complete description of the interaction between charged fermions and the electromagnetic field, forming the foundation for the theory of quantum electrodynamics.

1.1.1 Nonlinear Extensions of QED

Quantum Electrodynamics (QED) excels in describing electromagnetic interactions under typical conditions, where the fields involved are relatively weak. How-

ever, in extreme electromagnetic environments, such as those generated in high-intensity laser experiments or during heavy-ion collisions, the assumptions of linear field behavior in standard QED break down. Nonlinear effects, which arise due to quantum corrections like vacuum polarization and electron-positron pair creation, become significant. These effects are theoretically described by extending QED to include higher-order interactions, as encapsulated in the Heisenberg-Euler Lagrangian [35].

The Heisenberg-Euler Lagrangian for a constant electromagnetic field is given by:

$$\mathcal{L}_{\text{HE}} = -\frac{1}{4}F_{\mu\nu}F^{\mu\nu} + \frac{1}{8\pi^2}\int_0^\infty \frac{ds}{s^3}e^{-m^2 s}\left[(es)^2\coth(es) - \frac{(es)^2}{3} - 1\right], \qquad (1.2)$$

where e is the elementary charge, m is the electron mass, and s is a proper-time integration parameter. This expression is an effective field theory result that accounts for quantum corrections to the classical Maxwell equations due to virtual electron-positron pairs interacting with the electromagnetic field.

For weak fields, the Heisenberg-Euler Lagrangian can be expanded to yield an approximate form, where the quantum corrections become more transparent:

$$\mathcal{L}_{\text{HE}} \approx -\frac{1}{4}F_{\mu\nu}F^{\mu\nu} + \frac{\alpha^2}{90m^4}\left[(F_{\mu\nu}F^{\mu\nu})^2 + \frac{7}{4}(F_{\mu\nu}\tilde{F}^{\mu\nu})^2\right], \qquad (1.3)$$

where α is the fine-structure constant, and $\tilde{F}^{\mu\nu} = \epsilon^{\mu\nu\rho\sigma}F_{\rho\sigma}$ is the dual field intensity tensor. This approximate form highlights the nonlinear nature of QED, predicting effects such as photon-photon scattering, vacuum birefringence, and pair production in strong electromagnetic fields.

A key concept in nonlinear QED is the Schwinger limit, which defines the critical field intensity at which quantum vacuum effects become dominant. For electric fields, the Schwinger limit is given by:

$$E_{\text{c}} = \frac{m^2 c^3}{e\hbar} \approx 1.32 \times 10^{18} \text{ V/m}. \qquad (1.4)$$

$$B_{\text{c}} = \frac{m^2 c^2}{e\hbar} \approx 4.41 \times 10^9 \text{ T}. \qquad (1.5)$$

Figure 1 illustrates the propagation of a fermion in the presence of an intense magnetic field. When the external magnetic field is perturbatively incorporated into the fermion propagator, each insertion introduces a factor of $eB/m_e^2 = B/B_c$. The strength of the magnetic field compensates for the small coupling constant e, necessitating the inclusion of contributions up to infinite orders with respect to the external magnetic field. In this regime, where strong magnetic fields induce significant higher-order effects, the resulting physics exhibits non-perturbative and nonlinear behavior, commonly referred to as "nonlinear QED."

Exploring these nonlinear extensions of QED provides researchers with an opportunity to deepen our understanding of quantum field theory under extreme conditions, bridging theoretical advancements with experimental frontiers.
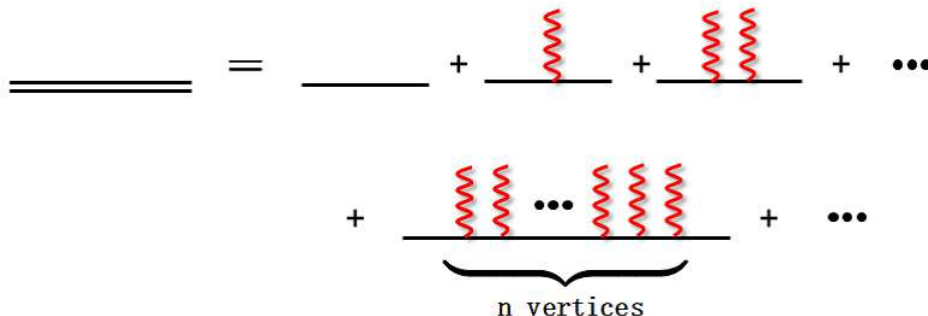
Figure 1: Dressed fermion propagator includes all the tree-level interactions with a vacuum polarization tensor in a strong external field

1.2   Quantum Chromodynamics (QCD)

Quantum Chromodynamics (QCD) is the fundamental theory describing the strong interaction, which binds quarks and gluons into hadrons such as protons and neutrons. As a non-Abelian gauge theory based on the SU(3) symmetry group, QCD differs significantly from Quantum Electrodynamics (QED), which is an Abelian theory. The gauge bosons of QCD, called gluons, mediate the strong force and possess a unique property: they themselves carry the color charge. This enables gluons to interact with each other, unlike the photons in QED, which are electrically neutral and do not interact among themselves.

The dynamics of QCD are encapsulated in its Lagrangian density, given by:

$$\mathcal{L}_{\text{QCD}} = \sum_q \bar{\psi}_{q,a}(i\gamma^\mu \partial_\mu - m_q)\psi_{q,a} - g_s \sum_q \bar{\psi}_{q,a}\gamma^\mu T^a_{ab}\psi_{q,b}A^a_\mu - \frac{1}{4}G^a_{\mu\nu}G^{a\mu\nu}, \quad (1.6)$$

where ψ_q represents the Dirac spinor for quarks of flavor q, with m_q being the quark mass, $D_\mu = \partial_\mu - ig_s T^a A^a_\mu$ is the covariant derivative, where g_s is the strong coupling constant, A^a_μ is the gluon field, and T^a are the SU(3) generators, and $G^a_{\mu\nu} = \partial_\mu A^a_\nu - \partial_\nu A^a_\mu + g_s f^{abc} A^b_\mu A^c_\nu$ is the gluon field intensity tensor, with f^{abc} being the structure constants of the SU(3) group. The QCD Lagrangian can be divided into three distinct parts. The first term describes the dynamics of free quarks, including their kinetic energy and masses. The second term captures the interaction between quarks and gluons, governed by the strong coupling constant g_s. Finally, the third term governs the dynamics of gluons and includes their self-interaction due to the non-Abelian nature of SU(3). The self-interaction of gluons arises from the nonlinear terms in the gluon field intensity tensor $G^a_{\mu\nu}$. These terms, proportional to $g_s f^{abc} A^b_\mu A^c_\nu$, lead to three-gluon and four-gluon vertices in Feynman diagrams. This self-interaction is a defining feature of QCD and is responsible for the unique properties of the strong interaction, such as confinement and asymptotic freedom.

One of the most remarkable properties of QCD is *asymptotic freedom*, which states that the intensity of the strong interaction becomes weaker at shorter

distances or higher energies. This phenomenon can be quantitatively described by the running of the strong coupling constant α_s with the squared momentum transfer Q^2:

$$\alpha_s(Q^2) \simeq \frac{12\pi}{(33 - 2N_f)\ln\left(Q^2/\lambda_{\text{QCD}}^2\right)}, \tag{1.7}$$

where N_f is the number of active quark flavors, and λ_{QCD} is the QCD scale parameter, typically around 200 MeV. At large Q^2, α_s becomes small, allowing perturbative techniques to be employed for calculations in high-energy processes such as deep inelastic scattering or jet formation in particle collisions.

At lower energies or larger distances, however, α_s increases significantly, leading to the phenomenon of *confinement*. This property ensures that quarks and gluons are never observed in isolation but are always confined within color-neutral hadrons. The confinement mechanism is often phenomenologically described by a potential between quarks:

$$V_s(r) = -\frac{4}{3}\frac{\alpha_s \hbar c}{r} + kr, \tag{1.8}$$

where the $1/r$ term dominates at short distances and resembles the Coulomb potential, while the linear term kr becomes significant at larger distances. Here, k is the string tension, a parameter characterizing the intensity of the confining potential.

When two quarks are pulled apart, the linear potential increases the energy of the system. Once the energy exceeds a critical threshold, it becomes energetically favorable to create a new quark-antiquark pair from the vacuum. This process results in the formation of two new color-neutral hadrons rather than isolating a single quark. This characteristic feature of QCD is a direct consequence of the non-Abelian nature of the SU(3) gauge symmetry and the self-interacting gluons.

QCD plays a crucial role in explaining phenomena across a wide range of energy scales, from the formation and structure of nucleons to the high-energy interactions observed in particle colliders. The interplay between asymptotic freedom and confinement underpins much of our understanding of the strong force and continues to drive experimental and theoretical research in particle physics.

1.3 Quark-Gluon Plasma (QGP)

Under normal conditions, quarks and gluons are confined within protons, neutrons, and other hadrons due to the strong interaction described by Quantum Chromodynamics (QCD). However, at extremely high temperatures or densities, this confinement can break down, leading to a state where quarks and gluons are no longer bound together. This deconfined state of matter is called Quark-Gluon Plasma (QGP), a concept first proposed by Bjorken [17].

Lattice QCD, a computational approach to solving QCD on a discrete space-time lattice, predicts that such a phase transition occurs at a critical temperature T_C of approximately $150 \sim 200$ MeV. At this temperature, the energy is sufficient to overcome the confining potential that normally binds quarks and gluons within
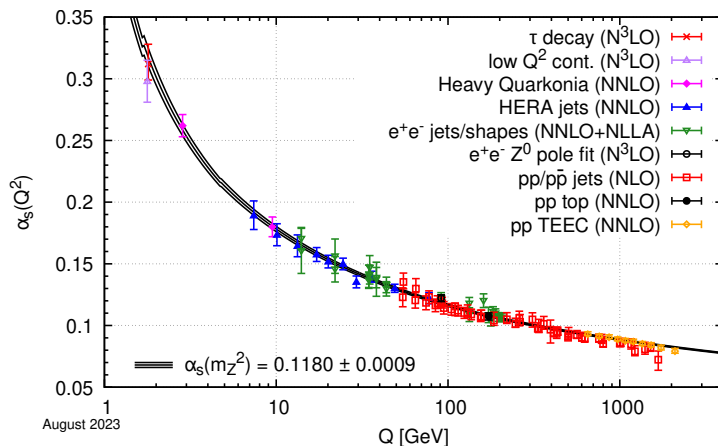
Figure 2: summary of α_s determinations as a function of energy scale Q, compared to the five-loop running of the coupling using the Particle Data Group average $\alpha_s(m_Z^2) = 0.1180 \pm 0.0009$ [36].

hadrons. As the system transitions from the hadronic phase to the QGP, the degrees of freedom increase significantly, resulting in a step-like behavior of the energy density normalized by the fourth power of the temperature, ϵ/T^4, as shown in Fig. 3 .

Phase transitions in general can occur in different ways: they can be a first-order transition, where the properties of the medium change abruptly, a second-order transition with continuous but rapid changes, or a crossover, where the change is smooth and gradual. Recent lattice QCD calculations suggest that the transition to QGP at low net baryon densities and high temperatures is a crossover [18, 14].

Figure 4 illustrates the phase diagram of QCD matter. The vertical axis represents the temperature, while the horizontal axis corresponds to the net baryon density normalized to the density of normal nuclear matter. This diagram shows regions corresponding to hadronic matter and QGP, as well as possible critical points or transition boundaries between these states. The QGP is believed to have existed naturally in the early universe, within the first few microseconds after the Big Bang, when temperatures were extraordinarily high. Understanding the QGP helps us probe the fundamental properties of the strong interaction and the behavior of matter under extreme conditions.

1.4   High-Energy Heavy-Ion Collisions and Space-Time Evolution

High-energy heavy-ion collisions provide a unique opportunity to study strongly interacting matter, particularly the quark-gluon plasma (QGP). When two highly Lorentz-contracted nuclei (such as gold at RHIC or lead at the LHC) collide, they overlap in a finite region of space, creating extremely hot and dense matter. The primary geometric parameter describing the collision is the *impact parameter b*, which is the transverse distance between the centers of the two colliding nuclei.
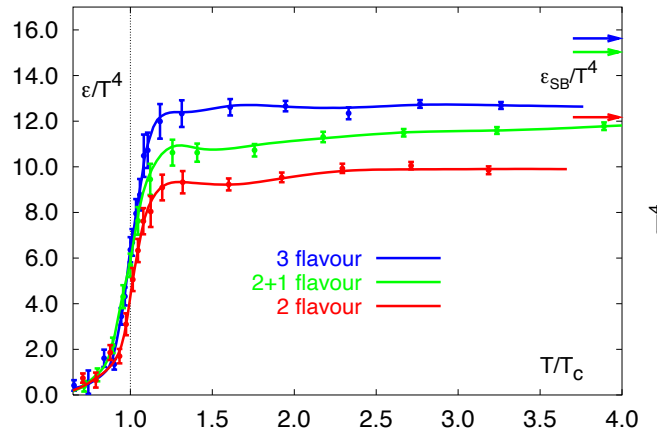
Figure 3: The energy density ϵ divided by 4th power of the temperature T^4 predicted bby lattice QCD [41]
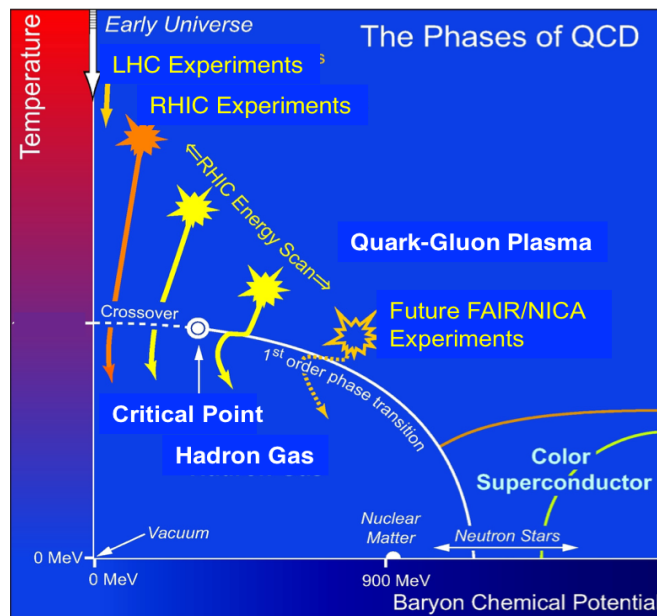
Figure 4: QCD phase diagram illustrating the region investigated by experiments. [50]

Although b itself is not directly measured, model calculations (e.g., the Glauber model [47]) can simulate the collision geometry and estimate:

- N_{part}: The number of *participants*, i.e., nucleons in the overlap region that actively interact.

- N_{coll}: The number of binary nucleon-nucleon collisions within the overlap region.

These quantities are of practical importance: N_{part} correlates with the volume of the interaction region, while N_{coll} helps in scaling particle production from hard scatterings.
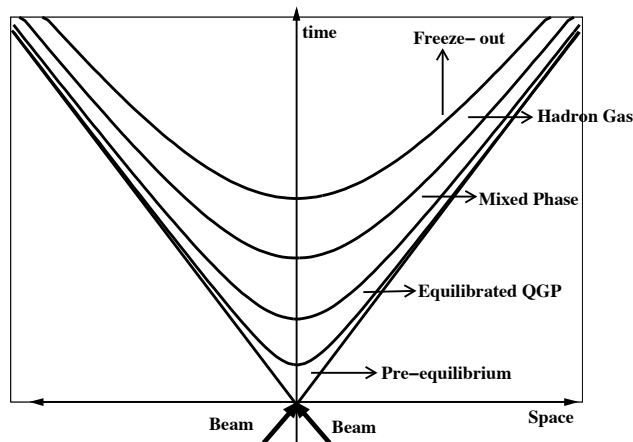
Figure 5: A schematic diagram of the space-time evolution in ultra-relativistic heavy-ion collisions. After an initial hard scattering phase and possible pre-equilibrium dynamics, a quark-gluon plasma (QGP) may form. As the system expands and cools, it transitions to a hadron gas and eventually freezes out. [57]

Figure 5 sketches a typical space-time evolution of a heavy-ion collision, high-lighting several key stages:

Pre-equilibrium Phase. At $t = 0$ and $z = 0$ (in the center-of-mass frame), two highly accelerated nuclei pass through each other. The overlap region is briefly energized by initial hard scatterings (e.g., parton-parton collisions) and attains a high energy density. This phase is often described by perturbative QCD parton cascades and is referred to as the pre-equilibrium stage. During this short period, the system rapidly evolves toward local thermal equilibrium.

Quark-Gluon Plasma (QGP). Once local thermal equilibrium is achieved, the system forms a quark-gluon plasma if the temperature (300–600 MeV) and energy density are sufficiently high. This QGP phase, expected to start around $\sim 0.6\,\text{fm}/c$ after the collision, can be described by relativistic hydrodynamics. In this state, quarks and gluons move relatively freely over distances larger than a typical hadron size, indicating deconfinement.

Mixed Phase and Hadronic Gas.   As the plasma expands, it cools. Eventually, the temperature falls below a critical value $T_C \approx 170\,\text{MeV}$, prompting a transition (hadronization) back to confined matter. Depending on the nature of the phase transition (crossover vs. first-order), a mixed phase may occur, where both partonic and hadronic degrees of freedom coexist. Lattice QCD suggests that the transition at zero or small net baryon density is a crossover, meaning thermodynamic variables change smoothly without a sharp phase boundary. After hadronization, the system becomes a hadronic gas, which continues to expand.

Freeze-out.   As the expansion persists, the temperature and density drop further to the *freeze-out* point ($T_F \approx 100\,\text{MeV}$). At this stage, inelastic collisions effectively cease, and the species of particles is fixed. A short time later, even elastic collisions end, causing the momentum distributions of the particles to "freeze out" (i.e., no further re-scattering). All final-state hadrons, photons, and leptons stream freely to the detectors, carrying information about the last scattering conditions.

High-energy heavy-ion collisions, therefore, provide a multi-stage dynamical system in which one can study the formation and properties of the QGP and trace the evolution of strongly interacting matter from partonic degrees of freedom to hadronic final states. The large initial energy densities, short time scales, and rapid expansion all combine to offer a fascinating glimpse into matter under extreme conditions.

1.5   Intense Electromagnetic Fields in High-Energy Heavy-Ion Collisions

When heavy ion (such as gold or lead) collide at extremely high energies in accelerators like the Relativistic Heavy Ion Collider (RHIC) or the Large Hadron Collider (LHC), they move at speeds close to the speed of light. In non-central collisions (where the colliding ions do not collide head-on, but rather pass each other slightly off-center), the large number of electric charges moving at these tremendous speeds can create extraordinarily intense magnetic fields as shown Fig. 6 [55, 61, 23].

The maximum intensity of the generated magnetic field can be on the order of 10^{14} T, corresponding to $|eB| \sim m_\pi^2$ [20] at the RHIC energy by applying the Biot-Savart law,

$$-eB_y \simeq 2Z\gamma\frac{e^2}{4\pi}(\frac{2}{b})^2, \tag{1.9}$$

where $v_z = \sqrt{1 - (2m_N/\sqrt{s_{\text{NN}}})}$ is the velocity of the nucleus, $/gamma = 1/\sqrt{1 - v_z^2}$ is the Lorentz factor of nucleus. At the LHC, these fields can be even larger ($|eB| \sim 10m_\pi^2$) [62, 63]. Here, m_π refers to the mass of the pion, a subatomic particle whose mass often serves as a natural reference scale in strong-interaction physics. These huge magnetic fields, however, exist for only a very short time —roughly the duration of the collision. Despite their short lifetimes, they allow researchers to explore how matter behaves under intense electromagnetic conditions, linking both QED and QCD in a single experimental setting.
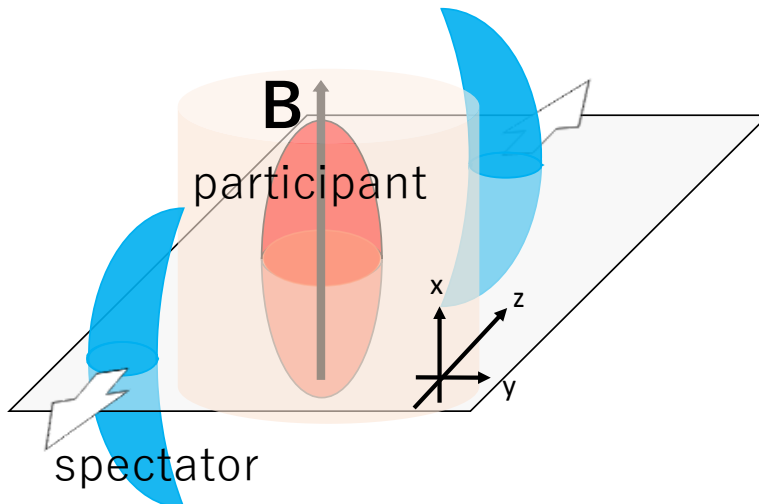
Figure 6: The schematic view of heavy-ion collision with electromagnetic fields generated by heavy-ion collision.

1.6   Phenomena Driven by Intense Magnetic Fields

Under these immense magnetic fields, many intriguing phenomena are predicted to occur according to both QED and QCD theories:

- **Schwinger mechanism**: If the magnetic field exceeds a critical strength of about 4.4×10^9 T, it can pull electron-positron pairs out of the vacuum, a process known as the Schwinger mechanism [53].

- **Photon splitting**: High-energy photons traveling through such fields can split into two lower-energy photons, illustrating the nonlinear nature of the QED vacuum [12].

- **Vacuum polarization**: Strong fields polarize the vacuum, meaning that the properties of empty space itself (as seen by photons) can change. One result is that virtual photons decay into lepton pairs in an anisotropic way (i.e., with a preferred direction).

- **Reduction of Critical temperature**: Lattice QCD studies suggest that intense magnetic fields might lower the temperature at which ordinary matter transitions into a quark-gluon plasma (QGP) [13, 21].

- **Chiral Magnetic Effect (CME)**: In the presence of a intense magnetic field, a medium where left-handed and right-handed quarks are imbalanced (chirally imbalanced) can exhibit charge separation along the field direction [28].

- **Quark synchrotron radiation**: Quarks moving in intense magnetic fields can emit synchrotron radiation, much like electrons in astrophysical contexts, potentially shedding light on quark dynamics within the QGP [58].
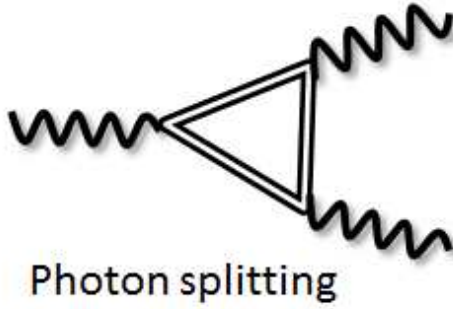
Figure 7: Feynman diagram of photon splitting in a strong magnetic field.

2 Phenomena in Strong Electromagnetic Fields

- **Schwinger Mechanism**: When the magnetic field exceeds a critical intensity 1.5, it can trigger the creation of real electron-positron pairs directly from the vacuum via tunneling, a process known as the Schwinger mechanism [53]. This phenomenon highlights the interplay between quantum tunneling and the energy provided by the external field. The magnetic field acts as a source, breaking the vacuum symmetry and enabling pair production at an energy scale defined by the field strength.

- **Photon Splitting**: High-energy photons traversing a strong magnetic field can split into two lower-energy photons. This process, known as photon splitting, occurs due to the interaction between the external field and virtual electron-positron loops [12]. While forbidden in free space, photon splitting becomes possible in the presence of intense fields. The underlying mechanism is shown in Fig. 7.

- **Reduction of Critical Temperature in QCD:** Lattice QCD studies suggest that intense magnetic fields reduce the critical temperature (T_c) for the phase transition from hadronic matter to quark-gluon plasma (QGP) [13, 21]. This effect is related to magnetic catalysis, where strong fields enhance chiral symmetry breaking, influencing the QCD vacuum structure and shifting the phase diagram under extreme conditions.

- **Chiral Magnetic Effect (CME):** In a chirally imbalanced medium subjected to a strong magnetic field, an electric current can be generated along the field direction due to the interplay between quantum anomalies and topological charge. This phenomenon, known as the chiral magnetic effect, provides a possible explanation for charge separation observed in heavy-ion collision experiments [28].

- **Quark Synchrotron Radiation:** Quarks moving in extreme magnetic fields undergo acceleration and emit synchrotron radiation, akin to electrons in astrophysical environments [58]. This radiation sheds light on energy loss mechanisms for quarks within the QGP and offers insights into the medium's electromagnetic properties and quark dynamics.
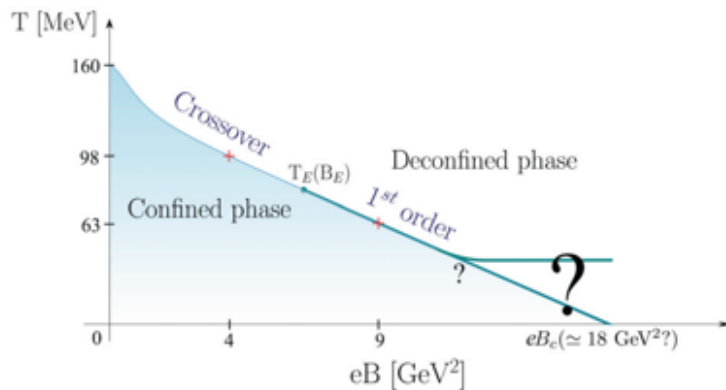
Figure 8: The critical temperature in QCD phase diagram in an external magnetic field. [21]

2.1 Experimental Signatures

Although these strong fields vanish rapidly, they can leave measurable footprints in the particles emerging from the collision. Some key observables include:

- **Global Polarization of Λ and $\bar{\Lambda}$**: The global polarization of Λ and $\bar{\Lambda}$ hyperons is one of the key observables for studying the interplay between strong vorticity fields and intense magnetic fields in heavy-ion collisions. The spin of these hyperons aligns with the angular momentum of the system, which is enhanced by the initial magnetic field. Measuring this polarization provides indirect evidence of the field strength and direction. The global polarization is typically reconstructed by analyzing the angular distribution of the daughter particles (protons and pions) from Λ decays in the hyperon rest frame.

- **Charge-Dependent Directed Flow**: Intense magnetic fields generated during the early stages of heavy-ion collisions can cause positively and negatively charged particles to experience different Lorentz forces, resulting in charge-dependent directed flow. This manifests as a difference in the directed flow parameter v_1 between particles of opposite charges. Such charge-dependent flow patterns can be particularly pronounced for heavy-flavor mesons, such as D and $\bar{D}$ mesons, due to their longer formation times and sensitivity to the early-time magnetic field [7, 3].

- **J/Ψ Polarization**: The polarization of J/Ψ mesons, which are formed by charm-anticharm quark pairs ($c\bar{c}$), provides a unique probe of the initial magnetic field configuration. In the presence of a strong magnetic field, the spin alignment of the charm quark pairs during the quarkonium formation can be affected. Studying the polarization of J/Ψ mesons in different kinematic regions and centrality classes allows researchers to infer the spatial and temporal evolution of the magnetic field. Such measurements require precision data and detailed theoretical modeling to disentangle contributions from the magnetic field and other sources, such as final-state interactions and medium-induced effects.

- **Charge Separation by the Chiral Magnetic Effect (CME)**: The Chiral Magnetic Effect (CME) predicts charge separation along the direction of the magnetic field in the presence of a chirally imbalanced medium. This phenomenon arises due to the coupling of the magnetic field with the chiral anomaly, leading to a net current of charges. Experimentally, the CME is studied by analyzing charge correlations and asymmetries in the final particle distributions. Detecting charge separation consistent with CME predictions would provide direct evidence of the role of magnetic fields in shaping the particle dynamics of the QGP. However, isolating the CME signal from background effects, such as local charge conservation and collective flow, remains a significant challenge. Advanced statistical and experimental techniques are being developed to enhance the sensitivity of such measurements.

2.2 Relevance to Fundamental Physics

Studying these extreme electromagnetic fields does more than reveal interesting features of heavy-ion collisions. It can also provide:

- **New Tests of QED and QCD**: Observing how matter behaves under fields of such strength can validate or challenge theoretical models, including high-order corrections in QED and the magnetic response of QCD matter.

- **Insights into the Early Universe**: Shortly after the Big Bang, similar (or even larger) field strengths may have existed. Understanding how strong fields affect matter in collisions can offer clues about processes in the early universe.

For detailed reviews on the physics of intense electromagnetic fields in heavy-ion collisions and related theoretical developments, see Refs. [33, 26] and references therein.

2.3 Direct Real/Virtual Photons

In high-energy heavy-ion collisions, photons (both real and virtual) are produced at every stage of the reaction. As electrically neutral particles, they interact only weakly with the surrounding medium after being emitted. This weak final-state interaction allows photons to escape the collision zone with minimal distortion of the information they carry. Consequently, *direct photons*, which do not originate from hadron decays, serve as essential probes of the hot and dense matter created in such collisions. Furthermore, intense electromagnetic fields (including magnetic fields) are expected to be generated in non-central collisions, and the direct photons produced in these early stages co-exist with these fields, potentially carrying information about the field strength and orientation.

Real photons are on-shell ($q^2 = 0$), meaning they satisfy the usual energy-momentum relation of massless particles. These photons can be detected by calorimeters in experiments. In contrast, virtual photons are off-shell ($q^2 > 0$) and
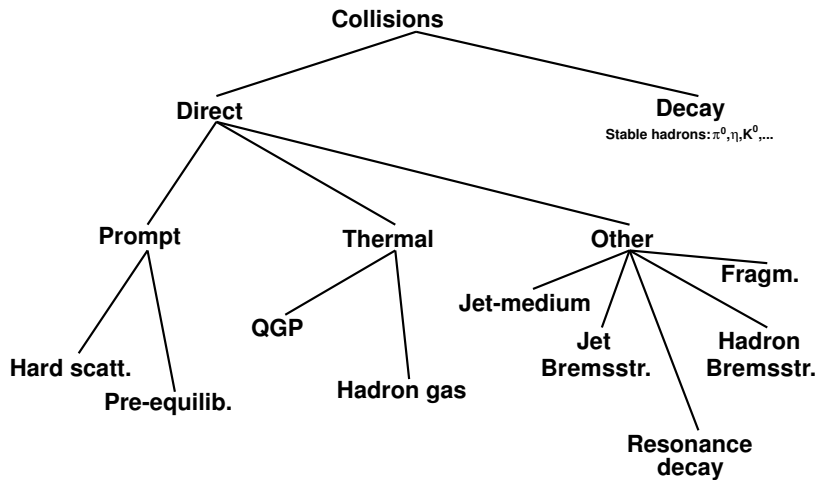
Figure 9: Schematic illustration of photon production processes in high-energy heavy-ion collisions [22]. Photons are emitted at all stages of the collision, providing information about the evolving system.

cannot be observed directly as free photons. Instead, they manifest in experiments through their decay products, often lepton pairs (e^+e^- or $\mu^+\mu^-$). Measuring these lepton pairs allows one to reconstruct the properties of the virtual photon (such as invariant mass and momentum). Both real and virtual photons are considered "direct" when they originate from partonic or early-time processes, rather than hadronic decays. An important theoretical link between the two channels is provided by the Kroll–Wada formula [44]:

$$\frac{dN_{\gamma^*\to l^+l^-}}{dm_{\mu\mu}} = \frac{2\alpha}{3\pi}\frac{1}{m_{\mu\mu}^2}\sqrt{1 - \frac{4m_\mu^2}{m_{\mu\mu}^2}}(1 + \frac{2m_\mu^2}{m_{\mu\mu}^2})SdN_\gamma, \tag{2.1}$$

where α is the fine-structure constant, m_e and m_{ee} are the mass of electron and electron pair, respectively, and S is a process dependent factor, including a from factor and a phase-space. This factor goes to 1 as $m_{ee} \to 0$ or $m_{ee} \ll p_\mathrm{T}$. This formula relates the yield of virtual photons (observed via lepton-pair production) to that of real photons. Although virtual photons do not emerge as free particles, they can be experimentally detected through their decay into lepton pairs (l^+l^-). By measuring these pairs and reconstructing their invariant mass and momentum, one can trace back to the kinematics of the off-shell (virtual) photon. This approach grants access to kinematic regions—particularly low-energy or low-p_T domains—where calorimeter-based detection of real photons proves challenging. Moreover, virtual photons help disentangle overlapping processes and probe the same physical sources (for instance, thermal radiation) that produce real photons. The PHENIX experiment at RHIC and the ALICE experiment at the LHC have both successfully measured virtual photon signals (via dileptons), confirming that such measurements provide crucial insights into the medium and its electromagnetic properties.

2.3.1 Production Mechanisms of Direct Photons

Figure 9 provides an overview of photon production in high-energy nuclear collisions. The yield of direct photons can be theoretically calculated using different frameworks, for example, perturbative QCD (pQCD) for prompt photons, hydrodynamic models for thermal photons, and transport or kinetic approaches for the pre-equilibrium stage [49, 51]. Below, we outline the main sources of direct photons, focusing on how they reflect different stages of the collision:

- **Prompt Photons**: At the earliest stage of the collision, parton-parton scattering (e.g., $q+g \rightarrow q+\gamma$ or $q+\bar{q} \rightarrow g+\gamma$, as shown in Fig. 10) generates high-energy photons, often referred to as prompt photons. These photons co-exist with the intense electromagnetic fields generated in non-central collisions and thus may carry signatures of those fields. In experimental analyses, the prompt-photon spectra from proton-proton collisions can be scaled by the number of binary collisions N_{coll} to estimate their contribution in heavy-ion collisions:

$$E\frac{dN^{\gamma}_{\text{scaled}}}{d^3p} \;=\; 6745\frac{\sqrt{s}}{p_{\text{T}}^5}\;\frac{N_{\text{coll}}}{\sigma_{pp}^{\text{in}}}, \qquad (2.2)$$

where σ_{pp}^{in} is the inelastic nucleon-nucleon cross section in picobarns (pb) [60]. Prompt photons dominate at high transverse momentum (p_{T}), where perturbative QCD (pQCD) calculations are generally reliable.
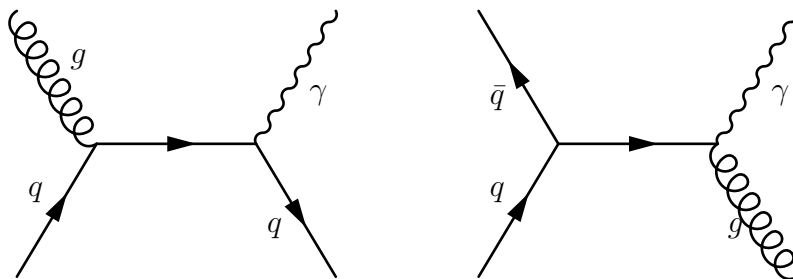
Figure 10: Feynman diagrams for (a) $q + g \rightarrow q + \gamma$ and (b) $q + \bar{q} \rightarrow g + \gamma$. These processes occur at the initial stage of heavy-ion collisions, producing high-energy (prompt) photons.

- **Thermal Photons**: As the quark-gluon plasma (QGP) forms and thermalizes, photons are produced from interactions among quarks and gluons (e.g., $q+g \rightarrow q+\gamma$). Because these emissions reflect the temperature of the medium, they are called thermal photons. Experimentally, their spectra can be approximated by an exponential $A \times \exp(-p_{\text{T}}/T_{\text{eff}})$, where T_{eff} is an effective temperature. For instance, PHENIX at RHIC reported $T_{\text{eff}} = 221 \pm 19^{\text{stat}} \pm 19^{\text{syst}}$ MeV in Au+Au collisions at $\sqrt{s_{\text{NN}}} = 200$ GeV [10, 9] as shown Fig. 11, while ALICE at the LHC found $T_{\text{eff}} = 297 \pm 12^{\text{stat}} \pm 41^{\text{syst}}$ MeV in Pb+Pb collisions at $\sqrt{s_{\text{NN}}} = 2.76$ TeV [8] as shown 12. Thermal photons
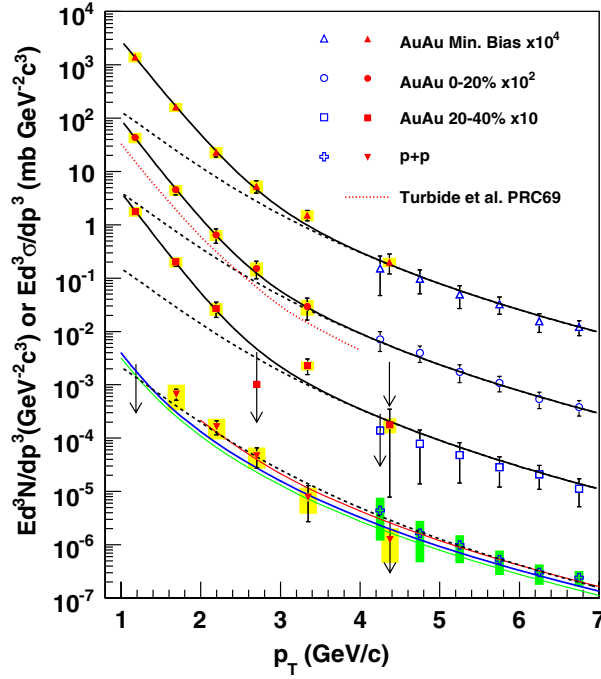
Figure 11: Direct photon spectra measured with virtual photon method in Au+Au collisions at $\sqrt{s_{\mathrm{NN}}} = 200$ GeV by the PHENIX experiment
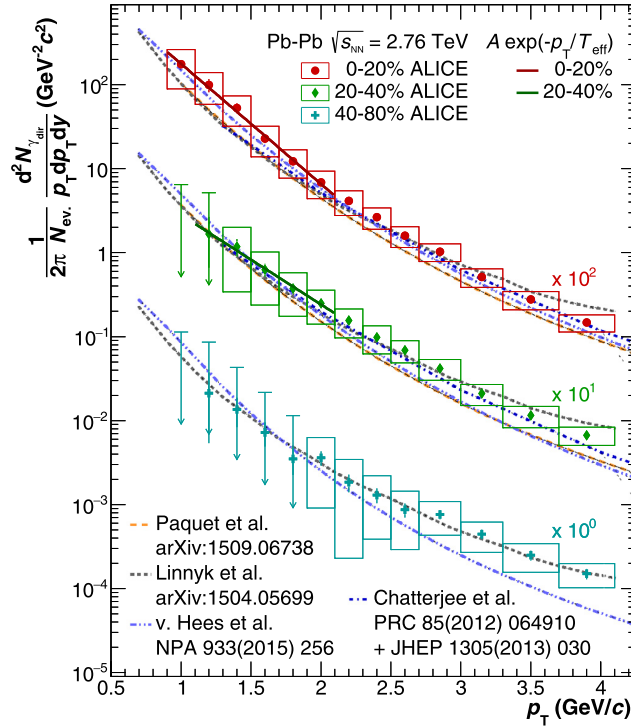
Figure 12: Direct photon spectra measured with virtual photon method in Pb-Pb collisions at $\sqrt{s_{\mathrm{NN}}} = 2.76$ TeV with the ALICE

can be real photons measured by calorimeters or can appear as virtual photons that decay into lepton pairs, allowing the same temperature extraction from dilepton spectra.

- **Pre-equilibrium Photons**: Before the system reaches local thermal equilibrium, collisions among partons in an off-equilibrium state can emit photons. These pre-equilibrium photons carry information about the early-time evolution, the approach to equilibration, and potentially the strongest magnetic fields present immediately after the collision.

Because these prompt photons (both real and virtual) are produced at early times, they co-exist with the intense magnetic fields generated in non-central collisions. Thus, the prompt photons may carry information about the intensity and spatiotemporal profile of the electromagnetic fields. Therefore, measuring direct real/virtual photons at LHC energies provides a valuable probe for studying both the hot QCD matter and the intense magnetic fields generated in high-energy heavy-ion collisions.

2.4 Organization of this thesis

This thesis explores virtual photon polarization as a new probe for the intense magnetic fields generated during high-energy heavy-ion collisions. The feasibility of measuring virtual photon polarization is evaluated using the statistical data collected during the first three operational phases with ALICE. Additionally, the thesis presents an analysis of the Pb – Pb collision data at $\sqrt{s_{\mathrm{NN}}} = 5.36$ TeV collected in 2023 This thesis is organized as following. Section 3 provides an overview of the LHC and the ALICE detector, highlighting their relevance to this study. Section 4 discusses the feasibility of measuring virtual photon polarization within the ALICE experiment, emphasizing the potential as a probe for intense magnetic fields. In Section 5, I presents the analysis of the Pb – Pb collision data at $\sqrt{s_{\mathrm{NN}}} = 5.36$ TeV taken in 2023. In Section 6, I show the results of measurement of the virtual photon polarization. Finally, the conclusion of this thesis in Section 7

3 Experimental Setup

3.1 Large Hadron Collider (LHC)

The Large Hadron Collider (LHC) is a two-ring superconducting hadron accelerator and collider located at CERN. The LHC is installed in the existing 26.7 km-long tunnel at CERN, situated on the border between France and Switzerland [25]. The tunnel of the LHC, located on the border of France and Switzerland, has a circumference of 26.7 km. It lies at depths ranging from 45 m to 170 m below the surface on the plane inclined by 1.4% towards Léman Lake. The LHC can collide protons at center-of-mass energy (CME) up to 14 TeV and lead ions up to 5.5 TeV per nucleon. Before Long Shutdown 2 (2019 – 2021, LS2), protons were generated by stripping electrons from hydrogen gas using an electric field

and then accelerated to 50 MeV by Linac2, which served as the injector for the Proton Synchrotron Booster (PSB). During LS2, to improve luminosity, Linac2 was upgraded to Linac4. Linac4 generates H^- ions from hydrogen gas and accelerates them along an 86 m linac comprising an RF quadrupole, a chopper line, an Alvarez drift tube linac (DTL), a cell-coupled drift tube linac (CCDTL), and a Pi-mode structure (PIMS), eventually reaching 160 MeV. Before injection into the PSB, the electrons are stripped from the H^- ions using a carbon foil, leaving a proton beam that is injected into the PSB. In the PSB, the beam is accelerated to 2 GeV, and in the Proton Synchrotron (PS), it is further accelerated to a maximum of 25 GeV. The beam is then sent to the Super Proton Synchrotron (SPS), where it reaches 450 GeV, before finally being accelerated to 6.8 TeV in the LHC.

The Large Hadron Collider (LHC) is a two-ring superconducting hadron accelerator and collider located at CERN, installed in a 26.7 km tunnel straddling the border of France and Switzerland [25]. The tunnel depth varies between 45 m and 170 m below ground level, following a plane inclined by about 1.4% toward Lake Léman. The LHC is designed to collide protons at center-of-mass energies (CME) up to 14 TeV and lead ions up to 5.5 TeV per nucleon.

Before Long Shutdown 2 (LS2, 2019–2021), protons were produced from hydrogen gas by stripping electrons using an electric field, then accelerated to 50 MeV by Linac2. During LS2, Linac2 was replaced by Linac4 to enhance luminosity. Linac4 generates H^- ions from hydrogen gas and accelerates them to 160 MeV using an 86 m linac that includes an RF quadrupole, a chopper line, an Alvarez drift tube linac (DTL), a cell-coupled drift tube linac (CCDTL), and a Pi-mode structure (PIMS). Prior to injection into the Proton Synchrotron Booster (PSB), a carbon foil strips electrons from H^-, leaving a proton beam. The beam then travels through the PSB, where it is accelerated to 2 GeV, and subsequently through the Proton Synchrotron (PS), where it reaches 25 GeV. It is then transferred to the Super Proton Synchrotron (SPS) and accelerated to 450 GeV. Finally, the beam is injected into the LHC, where it can reach energies up to 6.8 TeV per beam.

The process of preparing lead-ion beams for the LHC begins with a small piece of pure lead, about 2 centimeters long and weighing 500 milligrams. This lead sample is heated to approximately 500 degrees Celsius, causing a tiny fraction of the atoms to vaporize. An electric current is then used to strip a few electrons from each atom, turning them into ions that are ready to begin their journey through the accelerator complex.

The first stage in this journey is a linear accelerator known as Linac3. Here, the lead ions are given their initial energy boost, reaching about 4.5 MeV per nucleon. During this stage, additional electrons are removed from the ions, leaving them in a higher charge state, which makes it easier to accelerate them further. From Linac3, the ions move into the Low Energy Ion Ring (LEIR), a specialized circular accelerator designed to accumulate and increase the intensity of the lead-ion beam. In LEIR, the ions are further accelerated to an energy of 72 MeV per nucleon.

At this point, the ions transition from the unique ion-specific part of the

25
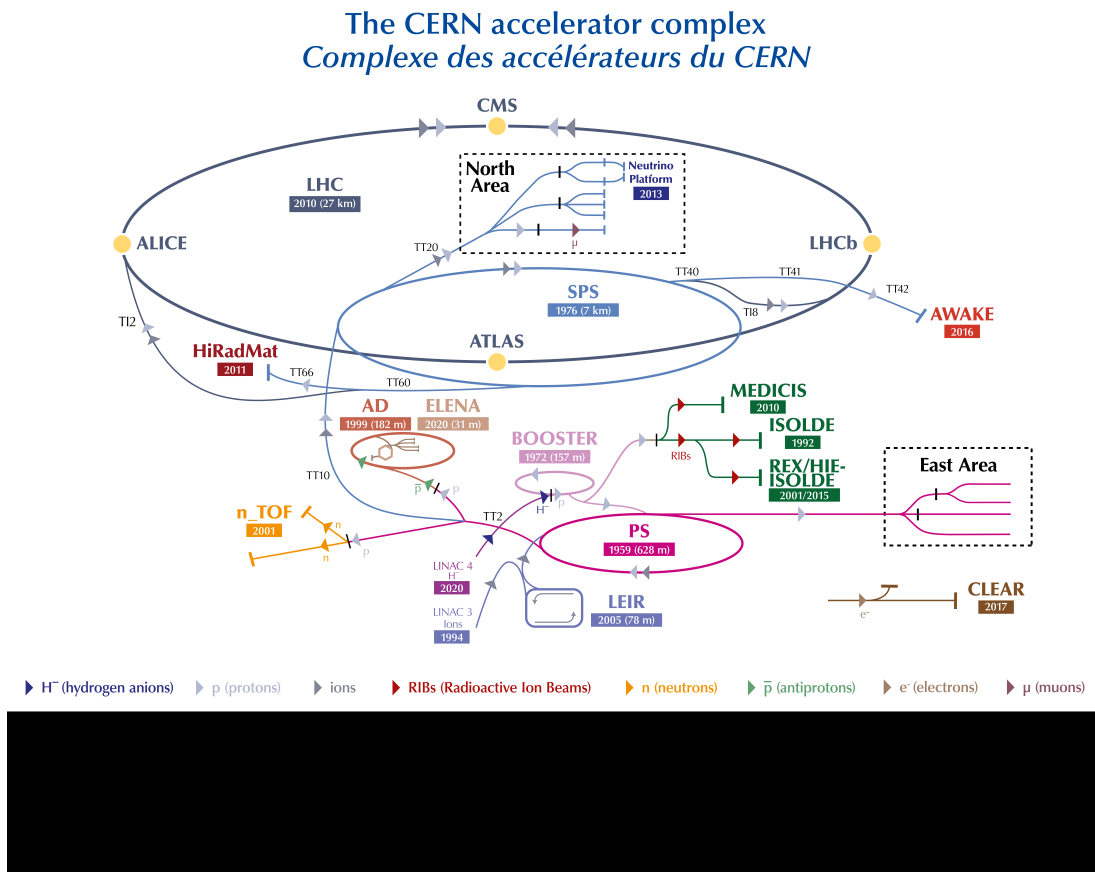
Figure 13: The CERN accelerator complex [46]

accelerator complex to the shared path used by both ions and protons. They first enter the Proton Synchrotron (PS), despite its name, which is also capable of accelerating heavy ions. In the PS, the lead ions are accelerated to an energy of 5.9 GeV per nucleon, and their last remaining electrons are stripped away, leaving them as fully ionized lead nuclei.

Next, the ions are transferred to the SPS, where they are further accelerated to 177 GeV per nucleon. Finally, the SPS injects the lead-ion beams into the LHC, where they are accelerated to their final energy—approximately 2.56 TeV per nucleon. This corresponds to a total collision energy of up to 5.5 TeV per nucleon pair when two lead-ion beams collide.

3.2   Overview of the ALICE apparatus

ALICE (A Large Ion Collider Experiment) is a dedicated heavy-ion physics detector at the LHC, designed to study QCD matter in collisions such as Pb–Pb at energies up to $\sqrt{s_{\mathrm{NN}}} = 5.36\,\mathrm{TeV}$. In central Pb–Pb events, as many as 8,000 charged particles can be produced. ALICE's subsystems collectively handle high multiplicity, provide extensive momentum coverage, and enable robust particle identification. Unlike other LHC experiments, ALICE runs a relatively low magnetic field (0.2–0.5 T) inside the L3 solenoid, which allows good acceptance of

1	**ACORDE**	ALICE Cosmic Rays Detector
2	**AD**	ALICE Diffractive Detector
3	**DCal**	Di-jet Calorimeter
4	**EMCal**	Electromagnetic Calorimeter
5	**HMPID**	High Momentum Particle Identification Detector
6	**ITS-IB**	Inner Tracking System - Inner Barrel
7	**ITS-OB**	Inner Tracking System - Outer Barrel
8	**MCH**	Muon Tracking Chambers
9	**MFT**	Muon Forward Tracker
10	**MID**	Muon Identifier
11	**PHOS / CPV**	Photon Spectrometer
12	**TOF**	Time Of Flight
13	**T0+A**	Tzero + A
14	**T0+C**	Tzero + C
15	**TPC**	Time Projection Chamber
16	**TRD**	Transition Radiation Detector
17	**V0+**	Vzero + Detector
18	**ZDC**	Zero Degree Calorimeter

Figure 14: Overview of The ALICE detectors in Run 3 [56]

very low-p_{T} tracks.

The LHC's third data-taking period (Run 3) follows the second Long Shutdown (LS2, 2019–2021). During this period, Pb–Pb collisions may reach $\sqrt{s_{\mathrm{NN}}} = 5.36\,\mathrm{TeV}$, and pp collisions can go up to $\sqrt{s} = 13.6\,\mathrm{TeV}$. ALICE, along with the other major LHC experiments, has undergone significant upgrades to enhance detector performance at higher collision rates and to increase sensitivity to rare physics processes. The primary goal is to record up to $\sim 10\,\mathrm{nb}^{-1}$ of Pb–Pb collisions (roughly 10^{11} interactions), with a continuous or near-continuous readout at 50 kHz in Pb–Pb and 200 kHz in pp. Large reference datasets in pp and p–Pb collisions will also be collected to isolate medium-specific effects in heavy-ion collisions.

3.2.1   Central Barrel

Although the central barrel forms the core region of ALICE (covering $|\eta| < 0.9$), it is summarized here only briefly. It comprises several crucial subsystems, each designed to cover a wide momentum range and to identify particles with high precision:

- **Inner Tracking System (ITS)**: Positioned closest to the beam axis, the ITS provides high-resolution vertexing and precision tracking for low-momentum charged particles. Consisting of seven concentric layers of silicon detectors, the upgraded ITS features reduced material budget and finer segmentation. This allows for better detection of secondary vertices (e.g. from charm or beauty decays) and improved efficiency in reconstructing low-p_{T} tracks.

- **Time Projection Chamber (TPC)**: The TPC is the primary tracking detector, offering three-dimensional charged-particle trajectory measurements over a large volume. By collecting ionization electrons drifting to the readout endplates, the TPC can reconstruct charged tracks with

excellent momentum resolution. The upgraded TPC now uses Gas Electron Multiplier (GEM) readout chambers to accommodate continuous data-taking at rates up to 50 kHz in Pb–Pb collisions. Together with the ITS, it provides robust charged-particle identification through energy-loss (dE/dx) measurements.

- **Time of Flight (TOF)**: Covering charged-particle identification in the intermediate momentum range (~ 0.2–$2.5\,\mathrm{GeV}/c$), the TOF system measures the arrival times of particles with an intrinsic timing resolution of tens of picoseconds. By correlating these times with the measured path length, ALICE can separate pions, kaons, and protons over a broad kinematic range.

- **Electromagnetic Calorimeters (EMCal)**: These sampling calorimeters detect electromagnetic showers from electrons, photons, and jets. EMCal and its extended DCal region are essential for jet-quenching studies (energy loss of partons in the quark–gluon plasma) and the identification of direct photons. The readout system has been upgraded to handle higher collision rates and to maintain fine spatial granularity for improved shower-profile measurements.

- **PHOton Spectrometer (PHOS)**: PHOS provides high-resolution measurements of photons over a smaller angular coverage than EMCal. Using high-granularity crystal modules and a charged-particle veto (CPV), PHOS can distinguish direct photons from those originating in neutral pion and η decays. This capability is crucial for probing thermal radiation from the QGP and searching for other rare photon-related signals.

All of these subsystems operate within the 0.2–0.5 T magnetic field of the L3 solenoid, originally from the LEP L3 experiment. The moderate field strength allows ALICE to track particles with both high and low transverse momentum. Upgrades introduced for Run 3 and beyond focus on improving the tracking resolution, raising the readout frequency to match higher collision rates, and enabling near-continuous data acquisition. More technical details on each detector can be found in Refs. [4].

3.2.2   Muon Detectors

The muon spectrometer is crucial for investigating quarkonia (e.g., J/ψ, Υ) and other muon probes of the hot, dense medium formed in heavy-ion collisions. By covering the pseudorapidity range $-4 \leq \eta \leq -2.5$ with the Muon Tracking Chambers (MCH) and Muon Identifier (MID), and $-3.6 \leq \eta \leq -2.45$ with the Muon Forward Tracker (MFT), ALICE gains sensitivity to heavy-flavor production and suppression patterns, as well as potential signals of the QGP.

- **Muon Chambers (MCH)**: The front-end electronics have been upgraded to sustain up to 100 kHz readout, ensuring compatibility with higher interaction frequencies. The MCH measures charged tracks emerging from the absorber, providing precise muon trajectory reconstruction.
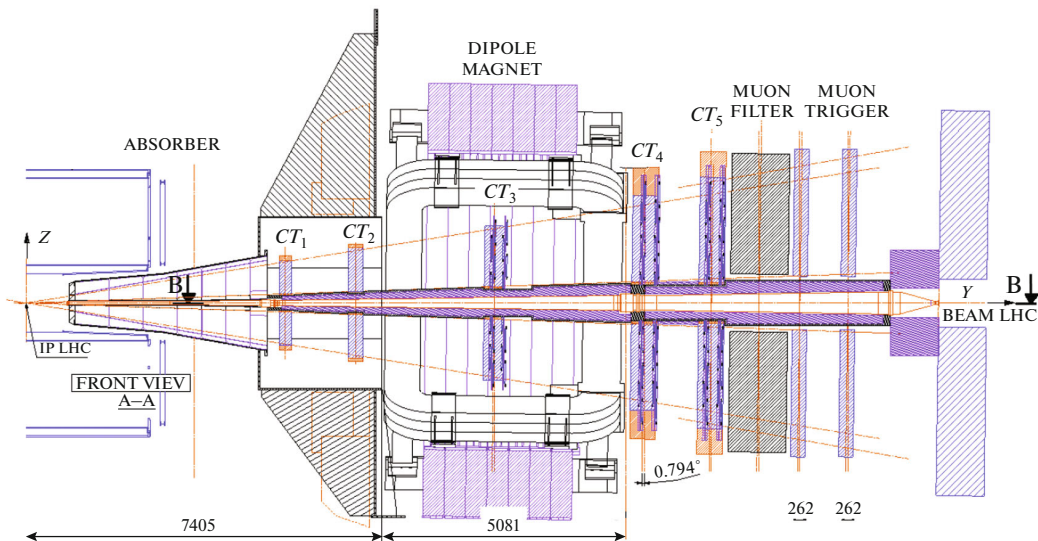
Figure 15: View of the muon spectrometer
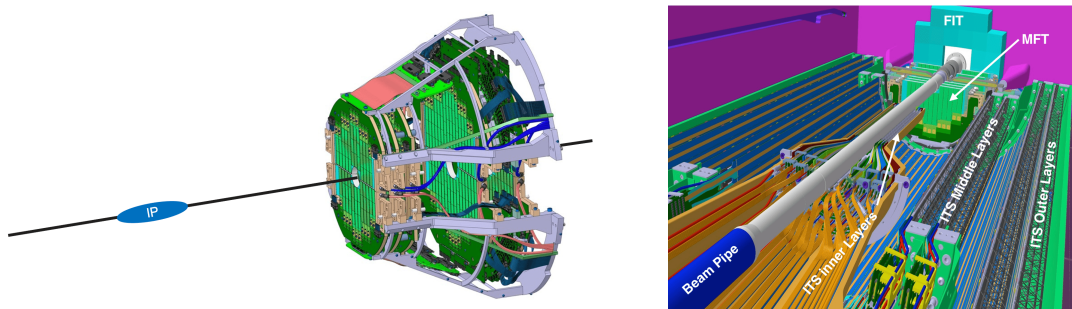
Figure 16: View of the Muon Forward tracker (MFT)

- **Muon Identifier (MID)**: Formerly referred to as the Muon Trigger Chambers, it now operates in a continuous or near-continuous mode with lower gain and newly developed front-end chipst. This system identifies muons by filtering out hadrons that fail to penetrate the absorber material.

- **Muon Forward Tracker (MFT)**: A newly installed detector placed before the front absorber, improving the precision of vertexing in the forward region. The MFT substantially enhances measurements of muon pairs, allowing detailed studies of heavy-flavor and vector-meson production in kinematic regions previously out of reach.

By running in continuous-readout mode, the muon detectors (MCH, MID, and MFT) can handle the higher collision rates of Pb–Pb (50 kHz) and pp (200 kHz). This increased data volume is vital for rare processes such as quarkonium suppression, regeneration, and flow studies in heavy-ion collisions.

Detector	z(mm)	$\eta_{\min}$	$\eta_{\max}$
FT0-A	3305	3.5	4.9
FT0-C	-843	-2.1	-3.3
FDD-A	17000	4.8	6.3
FDD-C	-19500	-4.9	-7.0
FV0	3160	2.2	5.0
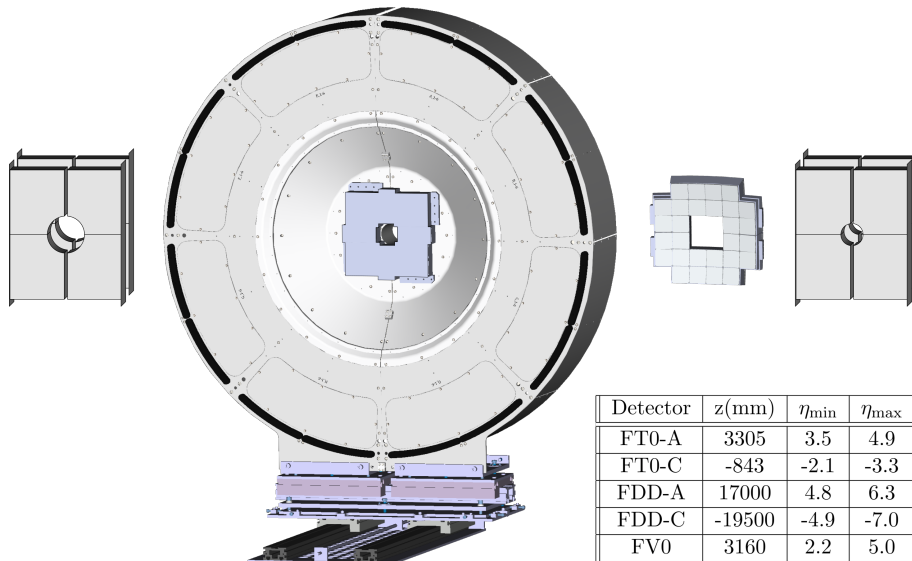
Figure 17: View of the FIT detectors illustrating the relative sizes of each component. From left to right FDD-A, FT0-A, FV0, FT0-C, and FDD-C are shown. Note that FT0-A and FV0 have a common mechanical support. FT0- A is the small quadrangular structure in the centre of the large, circular FV0 support. Note that all detectors are planar with the exception of FT0-C, which has a concave shape centered on the IP. The inset table lists the distance from the interaction point and the pseudorapidity coverage for each component.

3.2.3 Forward Detectors

ALICE's forward region complements the central barrel and muon systems by providing trigger signals, luminosity monitoring, multiplicity measurements at large $|\eta|$, and event-plane determination. These forward detectors enable ALICE to characterize global properties of each collision, distinguish diffractive and ultra-peripheral events, and measure background or beam-gas interactions. **Fast Interaction Trigger (FIT) [FIT]** Delivers rapid event triggers, monitors luminosity, provides initial vertex information, measures forward multiplicity, and tags diffractive/ultra-peripheral collisions. Operates with upgraded electronics for continuous or near-continuous readout. Replaces and extends the functionalities of the T0, V0, and AD detectors from Run 2.

- **Subcomponents:**

  1. **FT0**: Two arrays of quartz Cherenkov radiators (FT0-A and FT0-C), read out by MicroChannel Plate (MCP) photomultipliers. Achieves $\sim 25\,\mathrm{ps}$ time resolution per MIP, crucial for minimum-bias triggers and precise TOF start-time.

  2. **FV0**: A large, segmented scintillator disk with fiber-based light collection, covering forward pseudorapidity. Provides timing (single-MIP $\sigma_t \sim 200\,\mathrm{ps}$) and multiplicity data. Also helps generate fast triggers and centrality/event-plane estimates.

30

3. **FDD**: Two arrays of rectangular scintillator pads in overlapping layers. Covers large $|\eta|$ and detects single MIPs, making it ideal for diffractive and ultra-peripheral collision tagging. Also offers an independent centrality measurement in p–Pb and Pb–Pb collisions.

3.2.4 Online-Offline Computing system (O^2) [19]

The Online-Offline (O^2)system is a key ALICE upgrade for Run 3, enabling "continuous readout" of up to 50 kHz in Pb – Pb collisions and 200 kHz in pp or p – Pb. Rather than discarding entire events at the hardware trigger level, all detector signals stream to the computing facility, where real-time reconstruction algorithms compress raw data into compact objects (such as TPC clusters) on-the-fly. This approach significantly boosts the event statistics—potentially by a factor of 100 compared to earlier runs—while maintaining full reconstruction quality even under severe pile-up conditions. The software architecture integrates calibration, reconstruction, and offline analysis in a single framework, supported by local storage at Point 2 and additional resources on the Grid. By merging online and offline workflows, ALICE can collect and process vastly more collisions, which is vital for probing rare processes.

3.3 Basic kinematic variables in ALICE coordinates

The ALICE experiment uses a right-handed Cartesian coordinate system (x, y, z), centered at the interaction point (IP) with the origin at $(0, 0, 0)$. In this setup:

- The z-axis is aligned with the beam direction.

- The x-axis is defined to run from the IP toward the center of the LHC ring.

- The y-axis points upward.

Hence, the x–y plane is transverse (perpendicular) to the beam axis (z-axis). This choice ensures consistency across analyses within ALICE and with other LHC experiments.

In many physics analyses, coordinates are expressed in a spherical system (r, θ, φ):

$$
\begin{aligned}
r &= \sqrt{x^2 + y^2 + z^2}, \\
\theta &= \arctan\left(\frac{\sqrt{x^2 + y^2}}{z}\right), \\
\varphi &= \arctan\left(\tfrac{y}{x}\right).
\end{aligned}
\tag{3.1}
$$

Here, φ is the azimuthal angle around the beam (z) axis, measured from $\varphi = 0$ at $x = 0$ (the center of the LHC ring), and θ is the polar angle measured from the z-axis. To characterize particle emission along the beam axis in high-energy collisions, the rapidity y is often used:

$$
y = \tfrac{1}{2} \ln\left(\frac{E + p_z}{E - p_z}\right),
\tag{3.2}
$$

where E is the particle's total energy and p_z is the momentum component parallel to the z-axis. In the relativistic limit $(p \gg m)$, the pseudorapidity η frequently substitutes for y:

$$\eta = -\ln\bigl[\tan(\theta/2)\bigr], \tag{3.3}$$

where θ is the polar angle from above. Pseudorapidity is favored in certain detector analyses because it depends only on the emission angle and not on the particle's mass.

A particularly important momentum component in collider physics is the transverse momentum p_T, defined in the plane perpendicular to the beam:

$$p_T = \sqrt{p_x^2 + p_y^2} = p \sin \theta = \frac{p}{\cosh \eta}. \tag{3.4}$$

4 Feasibility study

4.1 Estimation of the Time Evolution of Intense Magnetic Fields Using a Resistive Relativistic Magneto-Hydrodynamics Model

In high-energy heavy-ion collisions, the quark–gluon plasma (QGP) that emerges can host significant electric currents, which in turn influence the external magnetic field [29]. Understanding these induced currents is crucial because they can extend the lifetime of the magnetic field well beyond its initial peak. To simulate this phenomenon, *relativistic magnetohydrodynamics* (RMHD) models have been introduced [30, 37, 38], but we employ a more advanced approach—**resistive relativistic magnetohydrodynamics** (RRMHD). This formalism incorporates a finite electrical conductivity for the QGP, as implied by results from Lattice QCD, perturbative QCD, and the AdS/CFT correspondence [2, 34, 45]. Such a non-zero conductivity dramatically affects both the strength and duration of the magnetic field, a key input for studies of polarization and related observables.

4.1.1 Milne Coordinates

In heavy-ion collisions, the fluid expands rapidly along the beam axis, and relativistic hydrodynamic simulations often face numerical instabilities at large space-time rapidities. To mitigate these issues, it is common to work in *Milne coordinates* (τ, x, y, η_s), defined by:

$$\tau = \sqrt{t^2 - z^2}, \quad \eta_s = \tfrac{1}{2} \ln\bigl(\tfrac{t+z}{t-z}\bigr). \tag{4.1}$$

Here, τ is the longitudinal proper time and η_s is the space-time rapidity. This choice leverages approximate boost invariance along the beam axis, which is a reasonable assumption at RHIC and LHC energies [**166**–**172**].

In these coordinates, the four-velocity transforms as follows:

$$
\begin{aligned}
u^\tau &= \cosh(\eta_s)\, u^t \;-\; \sinh(\eta_s)\, u^z, \\
u^{\eta_s} &= \frac{1}{\tau}\Bigl[-\sinh(\eta_s)\, u^t \;+\; \cosh(\eta_s)\, u^z\Bigr].
\end{aligned}
\tag{4.2}
$$

4.1.2 Resistive Relativistic Magnetohydrodynamics (RRMHD) Model

Simulating the magnetic field in a fast-expanding, conductive medium requires a comprehensive approach. We use a 3+1D resistive relativistic magnetohydrodynamics (RRMHD) model [48] to estimate the time evolution of these fields under realistic conditions:

- **Fluid Conservation Laws:** The baseline equations of ideal hydrodynamics remain:
$$\nabla_\mu N^\mu = 0, \nabla_\mu T^{\mu\nu} = 0, \tag{4.3}$$
  where N^μ is the fluid (baryon) current, $T^{\mu\nu}$ the energy-momentum tensor, and ∇_μ the covariant derivative.

- **Maxwell's Equations:**
$$\nabla_\mu F^{\mu\nu} = -J^\nu, \tfrac{1}{2}\nabla_\mu \epsilon^{\mu\nu\rho\sigma} F_{\rho\sigma} = 0, \tag{4.4}$$
  where $F^{\mu\nu}$ is the electromagnetic field tensor, J^μ is the electric current, and $\epsilon^{\mu\nu\rho\sigma}$ is the Levi-Civita tensor density.

- **Ohm's Law:**
$$J^\mu = q\,u^\mu + \sigma_e\,F^{\mu\nu}\,u_\nu. \tag{4.5}$$
  Here, σ_e is the electric conductivity (treated as a constant in this model), $q = -J^\mu u_\mu$ is the charge density in the fluid's comoving frame, and u^μ is the fluid four-velocity.

By including finite σ_e, our RRMHD model simultaneously incorporates the QGP's expansion and its non-zero conductivity, providing a self-consistent picture of how intense magnetic fields persist or decay.

Initial Conditions and Conductivity. We initialize the energy density using an optical Glauber approach, assuming the colliding nuclei move only along the beam (z) axis and are Lorentz-contracted in the transverse plane. Because we start hydrodynamics at $\tau = 0.2\,\mathrm{fm}/c$, the magnetic fields are already in a conductive QGP medium. The model calculates the initial fields by combining a scalar electric conductivity σ_e with the boosted Coulomb fields of the nuclei, following Refs. [48, 59]. While this approach simplifies the genuine pre-equilibrium dynamics (e.g., see [30] for a discussion of the difficulties in modeling pre-equilibrium EM fields), it still captures the essential evolution of B-fields in an expanding, conductive plasma. Consequently, we neglect magnetic-field-induced polarization before the QGP is established.

We separately checked the consistency of model parameters, finding it can describe relevant experimental data well. Nevertheless, we adopt an electric conductivity $\sigma_e \approx 0.46\,\mathrm{fm}^{-1}$ that is about an order of magnitude larger than typical LQCD or pQCD estimates. Although this higher value increases the field intensity at later times, we observe that our RRMHD model underestimates the electromagnetic-field strength if spectator contributions are omitted. Missing spectator currents lead to a smaller predicted B-field, and this larger σ_e partly compensates for that effect [48]. The full details of why and how this choice was made are beyond our current scope.

4.2   Time Evolution of Intense Magnetic Fields

We now illustrate the time dependence of the magnetic field using this RRMHD approach. Because the field strength decreases quickly from its initial maximum, capturing the temporal decay is crucial for computing polarization and other electromagnetic effects. Moreover, the field's initial intensity depends on the collision centrality, as the protons that remain spectators generate most of the field.

To maximize the initial field, we use a mid-central collision with an impact parameter of $b = 10$ fm, ensuring the hydrodynamics is still applicable. The RRMHD model is started at $\tau = 0.2$ fm/c under the same conditions (e.g. table 1 of Ref. [37]) that also provide realistic agreement with experimental observables. We extract the B_y component at the grid center where the energy density exceeds 0.15 GeV/fm^3, saving snapshots every 0.1 fm/c.
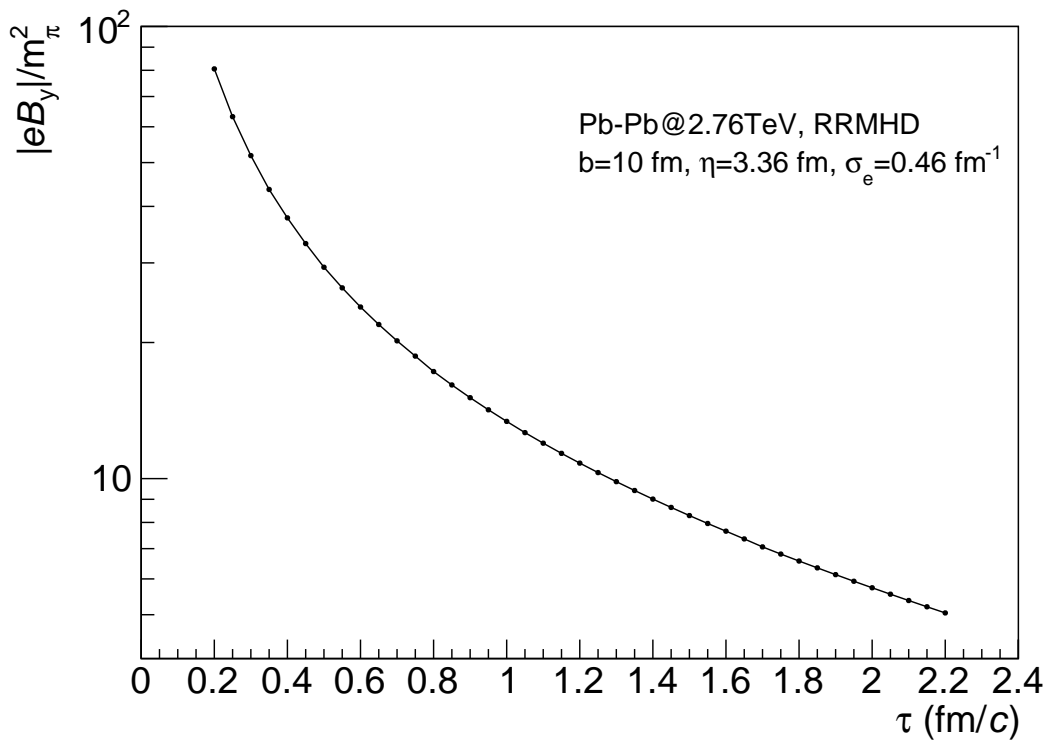
Figure 18:   Time evolution of B_y at the collision center from our RRMHD model [48] with $b = 10$ fm and $\sigma_e \approx 0.46$ fm^{-1}. This conductivity is larger than usual lattice estimates, compensating for omitted spectator currents that otherwise diminish the calculated field. Even under these conditions, the magnetic field rapidly decreases as the medium expands.

Figure 18 shows how B_y changes with proper time. Despite an initially large value, the field decays substantially within a few fm/c of the collision, underscoring the importance of a realistic time evolution model when calculating polarization or other magnetic-field-driven effects in QGP physics.
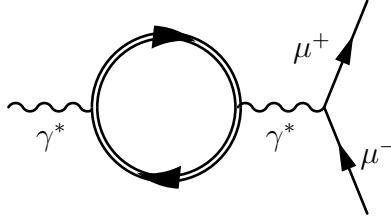
Figure 19: One-loop vacuum polarization diagram in the presence of an external magnetic field, leading to muon pair production.

4.3   Muon pair production rate asymmetry

In high-energy nuclear collision experiments, a intense external magnetic field can induce anisotropy in the production rate of muon pairs from virtual photons. This effect can be understood by considering the one-loop vacuum polarization diagram of a virtual photon with the infinite contribution of the magnetic field (Fig. 19). The infinite series of magnetic-field contributions (eB/m^2) in the one-loop polarization modifies the photon's polarization relative to the field direction, thus generating anisotropic responses in photon propagation [39].

I focused on this phenomenon as a factor that induces anisotropy in the muon pair production rate. The production rate is given by:

$$R_{\mu^+\mu^-} = \frac{\alpha^2}{2\pi^4}\, \mathrm{L}^{\mu\nu}(p_1, p_2)\, \mathrm{D}_{\mu\alpha}(q, eB)\, \mathrm{D}^*_{\nu\beta}(q, eB)\, \frac{\mathrm{Im}\mathrm{G}^{\alpha\beta}_R(q, T, eB)}{\mathrm{e}^{q^0/T} - 1}, \qquad (4.6)$$

where α is the fine-structure constant, e is the electric charge, $B = |\mathbf{B}|$ is the magnitude of the magnetic field, and T is the system temperature. p_1 and p_2 are the muon and anti-muon four-momentum, q is the virtual photon momentum satisfying $q = p_1 + p_2$. The leptonic tensor, $\mathrm{L}^{\mu\nu}$ is given by

$$\mathrm{L}^{\mu\nu} = p_1^\mu p_2^\nu + p_1^\nu p_2^\mu - \left(p_1 \cdot p_2 + m_\mu^2\right) g^{\mu\nu}, \qquad (4.7)$$

where m_μ is the muon mass and $g^{\mu\nu} = \mathrm{diag}(1, -1, -1, -1)$ is the metric tensor. The virtual photon source term $\mathrm{Im}\mathrm{G}^{\alpha\beta}_R(q, T, eB)/(\mathrm{e}^{q^0/T} - 1)$ contains the retarded Green function of the electric currents in the thermal and magnetic fields. Since it is difficult to show the details of the virtual photon source in high-energy heavy-ion collision, we replace it with the current conservation form as

$$\frac{\mathrm{Im}\mathrm{G}^{\alpha\beta}_R(q, T, eB)}{\mathrm{e}^{q^0/T} - 1} = \left(-g^{\alpha\beta}q^2 + q^\alpha q^\beta\right)C, \qquad (4.8)$$

where C is a constant. The effect of the polarization of the photon source term is partially canceled in the polarization ratio for the anisotropy. The photon propagator $\mathrm{D}_{\mu\nu}(q, eB)$ is given by

$$\mathrm{D}_{\mu\nu}(q, eB) = -\frac{i}{q^2}\left[g^{\mu\nu} - \frac{1}{q^2}\Pi^{\mu\nu}(q, eB)\right]^{-1}, \qquad (4.9)$$

where $\left[A^{\mu\nu}\right]^{-1}$ means the matrix inverse of the tensor $A^{\mu\nu}$. The vacuum polarization tensor $\Pi^{\mu\nu}$ is evaluated at one-loop level in the Furry picture with a constant

intense magnetic field, and evaluated numerically in the Landau summation form [32, 39]. We consider the contribution of electron and muon for virtual fermions included in the polarization tensor.

4.4   Vacuum polarization tensor in constant external intense magnetic field

The vacuum polarization tensor with the effect of an intense external magnetic field in it, $\Pi^{\mu\nu}$, is given by [11].

$$\Pi^{\mu\nu}(k) = (\mathrm{P}^{\mu\nu} - \mathrm{P}^{\mu\nu}_{\parallel} - \mathrm{P}^{\mu\nu}_{\perp})\mathrm{N}_0(k) + \mathrm{P}^{\mu\nu}_{\parallel}\mathrm{N}_1(k) + \mathrm{P}^{\mu\nu}_{\perp}\mathrm{N}_2(k), \tag{4.10}$$

where, $\mathrm{N}_i(\mathrm{i} = 0, 1, 2)$ are form factors, k^μ is the photon four-momentum and the projection tensors are defined by

$$\mathrm{P}^{\mu\nu} = k^2 \eta^{\mu\nu} - k^\mu k^\nu, \ \ \mathrm{P}^{\mu\nu}_{\parallel} = k_{\parallel}^2 \eta^{\mu\nu} - k_{\parallel}^\mu k_{\parallel}^\nu, \ \ \mathrm{P}^{\mu\nu}_{\perp} = k_{\perp}^2 \eta^{\mu\nu} - k_{\perp}^\mu k_{\perp}^\nu. \tag{4.11}$$

The direction of the magnetic field is the y-axis direction in a right-handed coordinate system. k^μ and the metric tensor $\eta^{\mu\nu}$ are defined in the direction with respect to the magnetic field as follows.

$$k_{\parallel}^\mu = (k^0, 0, k^2, 0) = (\omega, 0, k_y, 0), \ \ k_{\perp}^\mu = (0, k^1, 0, k^3) = (0.k_x, 0, k_z) \tag{4.12}$$

$$\eta_{\parallel}^{\mu\nu} = \mathrm{diag}(1, 0, -1, 0), \ \ \eta_{\perp}^{\mu\nu} = \mathrm{diag}(0, -1, 0, -1) \tag{4.13}$$

$$k_{\parallel}^2 = \omega^2 - k_y^2 \tag{4.14}$$

$$k_{\perp}^2 = -(k^1)^2 - (k^3)^2 = -\mathbf{k}_{\perp}^3 \tag{4.15}$$

The form factor N_i (i=0,1,2) in eq.(4.10) is given by

$$\mathrm{N}_i = -\frac{\alpha}{4\pi} \int_{-1}^{1} dv \int_{0-i\epsilon}^{\infty-0\epsilon} [\tilde{\mathrm{N}}_i(y, v) e^{-i\psi(z,v)\eta - i\phi(v;r,\mu)} - \frac{1-v^2}{y} e^{-i\frac{y}{\mu}}] dy, \tag{4.16}$$

$$\tilde{\mathrm{N}}_0(y, v) = \frac{\cos(vy) - \mathrm{ccot}(y)\sin(vy)}{\sin(y)}, \tag{4.17}$$

$$\tilde{\mathrm{N}}_1(y, v) = (1 - v^2)\cot(y), \tag{4.18}$$

$$\tilde{\mathrm{N}}_2(y, v) = 2\frac{\cos(vy) - \cos(y)}{\sin^3(y)}, \tag{4.19}$$

$$\psi(y, v) = \frac{\cos(vy) - \cos(y)}{\sin(y)}, \tag{4.20}$$

$$\phi(v; r, \mu) = \frac{1 - (1 - v^2)r}{\mu}, \tag{4.21}$$

where the dimensionless quantities μ, r, and η are defined as follows

$$\mu = \frac{eB}{m^2}, \quad r = \frac{k_{\parallel}^2}{4m^2}, \quad \eta = \frac{2q}{\mu} \quad \text{where,} \quad q = \frac{\vec{k}_{\perp}^2}{4m^2} \tag{4.22}$$

Since it is a complicated double integral as in Eq.4.16, analytical calculations have been difficult. Calculations have been performed only under limited conditions, such as the red and green regions in Fig.20 [24, 40, 27].

In 2012, K. Hattori and K. Itakura derived the complete sum of Landau levels for the photon vacuum polarization tensor in a constant external magnetic field at the one-loop level, originating from fermion-antifermion pairs [43]. In this process, a double series over n and l is obtained by expansion. Here, n and l correspond to the Landau levels of virtual fermions confined in the external magnetic field and are the indices in the one-loop diagram. In 2013, Ishikawa et al. obtained a tabular form of the sum of Landau levels that is easily renormalized for the evaluation of the vacuum polarization tensor in the LHC energy region [39]. The form factor in Eq. 4.16 has already been renormalized, so it cannot be calculated numerically. This expression can be split into two terms: $r \neq 0$ (first term) and $r = 0$ (second term), as shown in Eq. 4.23.

$$\begin{aligned} N_j = \; & - \; \frac{\alpha}{4\pi} \int_{-1}^{1} dv \int_{0-i\epsilon}^{\infty-0\epsilon} [\tilde{N}_j(y,v) e^{-i\psi(y,v)\eta} (e^{-i\phi(v;r,\mu)} - e^{-i\frac{y}{\mu}})] dy \\ & - \; \frac{\alpha}{4\pi} \int_{-1}^{1} dv \int_{0-i\epsilon}^{\infty-0\epsilon} [(\tilde{N}_j(y,v) e^{-i\psi(y,v)\eta} - \frac{1-v^2}{y}) e^{-i\frac{z}{\mu}})] \end{aligned} \tag{4.23}$$

The first term is transformed into a series using the method of [43], while the second term is analytically connectable.

$$\begin{aligned} N_j = \; & - \; \frac{\alpha}{4\pi} \sum_{n=0}^{\infty} C_n \sum_{l=0}^{\infty} \Omega_{lj}^n(r,\eta,\mu) \\ & - \; \frac{\alpha}{4\pi} \int_{-1}^{1} dv \int_{0-i\epsilon}^{\infty-0\epsilon} [(\tilde{N}_j(y,v) e^{-i\psi(y,v)\eta} - \frac{1-v^2}{y}) e^{-i\frac{y}{\mu}})] \end{aligned} \tag{4.24}$$

In the presence of a strong external magnetic field, when pair production occurs, the final state particles are confined in the magnetic field, so their energies are determined by the Landau levels. The kinematic condition for pair production is that the photon's longitudinal momentum r must exceed the Landau levels, which is given by:

$$r = \left\{ \sqrt{m^2 + 2leB} + \sqrt{m^2 + 2(1+n)eB} \right\}^2 \tag{4.25}$$

Here, n and l are the Landau levels, and r is the longitudinal momentum of the photon.

Thus, all regions of Fig. 20 can be numerically verified. The line in Fig. 20 represents the threshold at which a photon decays into a fermion-antifermion pair. The photon decays when its longitudinal momentum exceeds the right-hand side of Eq. 4.25, and this value is determined by the Landau levels.
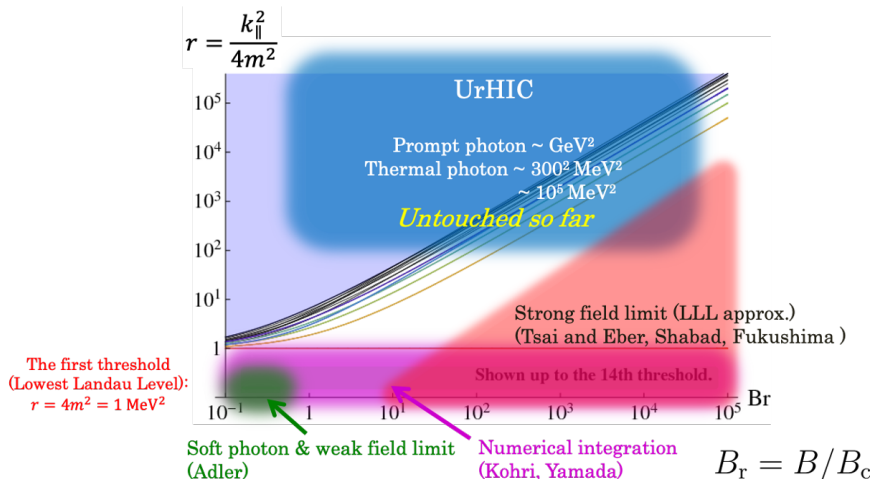
Figure 20: The region in which the theoretical interpretation of the vacuum polarization tensor is obtained in terms of the photon longitudinal momentum and the intensity of the magnetic field [31].

4.5   Definition of calculated Virtual photon polarization

To define the virtual photon polarization in the context of high-energy heavy-ion collisions, we consider the coordinate system depicted in Fig. 21. This coordinate system provides the geometric foundation for polarization calculations and plays a crucial role in expressing the relationship between particle momenta and the direction of the external magnetic field.

Here, the z-axis is aligned with the beam axis of the heavy-ion collision, and the x-z plane is defined as the event plane. The magnetic field is oriented along the y-axis, reflecting its perpendicular alignment to the event plane in non-central collisions. This configuration also accounts for the rotational symmetry of particle production rates within the x-z plane.

Within this coordinate system, the momenta of the muon and anti-muon are defined as $\mathbf{p}_1$ and $\mathbf{p}_2$, respectively. Based on this, we introduce the normal vector to the decay plane of the muon pair, $\mathbf{n}_{\mu\mu}$, which is defined by the following equation:

$$\mathbf{n}_{\mu\mu} = \frac{\mathbf{p}_1 \times \mathbf{p}_2}{|\mathbf{p}_1 \times \mathbf{p}_2|} \tag{4.26}$$

Next, $\mathbf{n}_{\mathrm{ref}}$ is a vector orthogonal to the magnetic field, defined based on the virtual photon's momentum as follows:

$$\mathbf{n}_{\mathrm{ref}} = \frac{(\mathbf{p}_1 + \mathbf{p}_2) \times (\mathbf{p}_1 + \mathbf{p}_2)_{xz}}{|(\mathbf{p}_1 + \mathbf{p}_2) \times (\mathbf{p}_1 + \mathbf{p}_2)_{xz}|} \tag{4.27}$$

Finally, we consider the angle θ between the magnetic field $\mathbf{B}$ and the decay plane's normal vector $\mathbf{n}_{\mu\mu}$. This angle is given by:

$$\theta = \cos^{-1}(\mathbf{n}_{\mu\mu} \cdot \mathbf{n}_{\mathrm{ref}}) \tag{4.28}$$

Using this coordinate system, the polarization of the virtual photon, P_{cal}, is
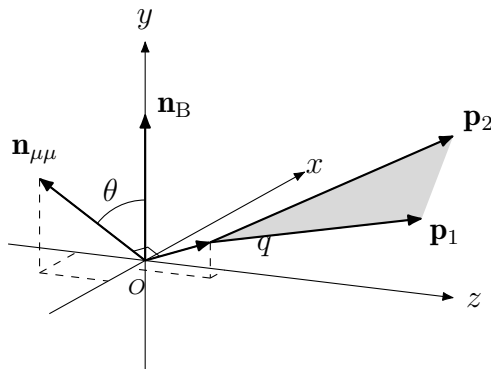
Figure 21: The definition of the angle between decay plane of muon pair and the intense magnetic field. $\mathbf{p}_1$ and $\mathbf{p}_2$ are momentum of μ^- and μ^+. The vector $\mathbf{n}_B$ is the unit vector of $\mathbf{B}$, and $\mathbf{n}_{\mu\mu}$ is the unit vector of the decay plane of muon pair which is determined by $\mathbf{p}_1$ and $\mathbf{p}_2$.

defined based on the muon pair production rates as:

$$P_{\text{cal}} = \frac{R_\perp - R_\parallel}{R_\perp + R_\parallel} \tag{4.29}$$

Here, $R_\perp$ denotes the muon pair production rate when $\theta = \pi/2$ (perpendicular to the magnetic field), and $R_\parallel$ represents the production rate when $\theta = 0$ (parallel to the magnetic field).

In numerical calculations, these production rates are evaluated by incorporating the intensity of the magnetic field based on the model. The results will be discussed in the next section, along with details about the experimental setup, the time evolution of the magnetic field, and the kinematics of the muons.

This analysis reveals the role of the external magnetic field in determining the polarization of the virtual photon and how the geometry of the decay process influences its polarization characteristics.

4.6   Calculation setup

To numerically evaluate the polarization of the virtual photon, P_{cal}, it is essential to appropriately define the virtual photon's four-momentum and its geometrical configuration. These settings significantly influence the physical interpretation of the results and their consistency with experimental observations.

The virtual photon's mass is chosen based on the following considerations. As shown in Fig. 22 [42], P_{cal} tends to increase as the virtual photon's mass decreases. However, for muon pair production to occur, the squared mass of the virtual photon, q^2, must exceed $(210 \text{ MeV}/c^2)^2$. Considering this threshold and the experimental preference for lighter virtual photons due to higher production yields, we set $q^2 = (300 \text{ MeV}/c^2)^2$. This value is physically meaningful and ensures consistency with experimental conditions.

The geometrical configuration of the virtual photon's momentum is defined based on experimental observations. In high-energy heavy-ion collisions, the total
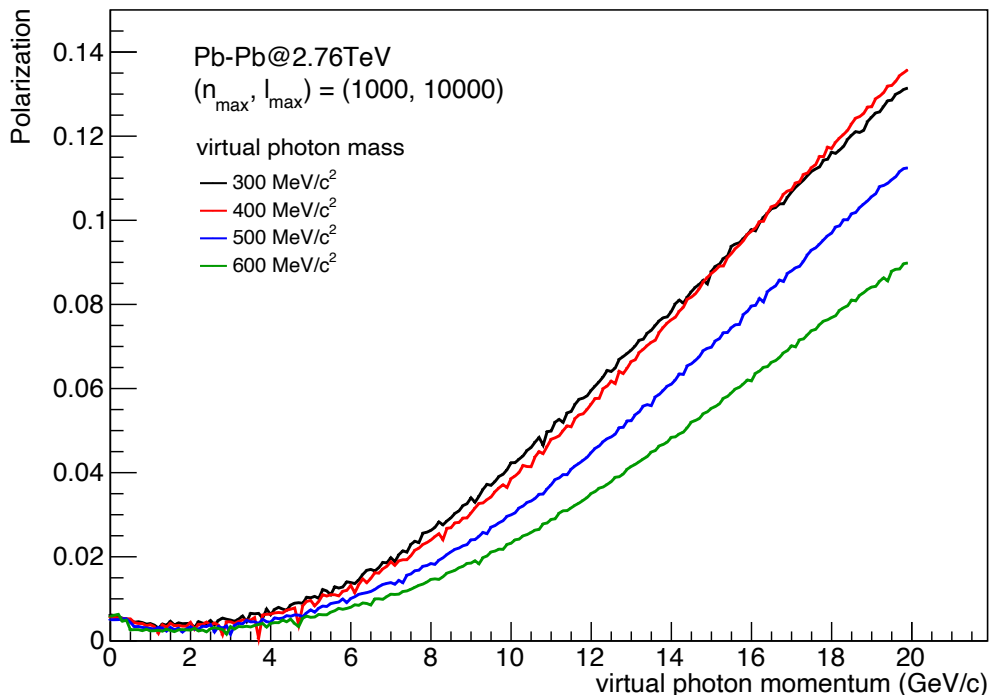
Figure 22: Mass dependence of virtual photon polarization

momentum of the produced muon pairs is predominantly aligned with the beam axis (z-axis) within the acceptance range of the ALICE experiment's muon spectrometer ($2.5 < |\eta| < 4.0$) [1]. To simplify the configuration while maintaining realism, we assume the virtual photon propagates along the z-axis.

To compute P_{cal}, we first determine the magnetic field intensity and substitute it into the formula for the muon pair production rate (Eq. (4.6)). This allows the calculation of the production rate perpendicular to the magnetic field, $R_\perp$, and the production rate parallel to the magnetic field, $R_\parallel$. These rates are then used in the definition of the polarization (Eq. (4.29)) to obtain P_{cal}.

For the calculation of the vacuum polarization tensor, convergence is ensured by imposing an upper limit on the Landau level summation. Following Ref. [39], we fix $l_{\max} = 1 \times 10^4$ and validate the dependence on $n_{\max}$. As a result, $(n_{\max}, l_{\max}) = (1 \times 10^3, 1 \times 10^4)$ is used, ensuring both the accuracy and convergence of the numerical calculations.

To evaluate the expected P_{cal} with the ALICE detector, we have to perform an averaging processes on the theoretical $\langle P_{\mathrm{cal}} \rangle$ according to detector limitations and a realistic initial virtual photon production rate. Experimentally the time resolution is not precise enough to detect rapid changes in the muon pair production rate, so we have to average over a time range for the prompt virtual photon decays. To fix the time range for prompt photon production, we employ $0.2 < \tau < 0.7$ fm/c from the lifetime of prompt virtual photons estimated to be $\tau > \hbar/(M_{\gamma^*} c^2) \simeq 0.7$ fm/c based on the uncertainty principle.

Parameter	Value/Condition
Virtual photon mass, q^2	$(300 \text{ MeV}/c^2)^2$
Virtual photon's three-momentum	$(0, 0, p_z)$ (aligned with z-axis)
Acceptance range of ALICE detector	$-4.0 < \eta < -2.5$
Production rate perpendicular to $\mathbf{B}$, $R_\perp$	$\theta = \pi/2$
Production rate parallel to $\mathbf{B}$, $R_\parallel$	$\theta = 0$
Landau level summation limits	$(n_{\max}, l_{\max}) = (1 \times 10^3, 1 \times 10^4)$
Time range	$0.2 < \tau < 0.7 \text{ fm}/c$

Table 1: Summary of the calculation setup for evaluating the virtual photon polarization P_{cal}.

4.7 Uncertainty

To estimate how momentum-resolution uncertainties affect our final polarization values, we applied a "smearing" method for each momentum bin. Specifically, we assumed that the momentum in a given bin is normally distributed with a standard deviation of $0.25 \text{ GeV}/c$, reflecting our detector's approximate resolution for this analysis. For each momentum value, we drew 10 random samples from this Gaussian distribution and recalculated the polarization for each sampled momentum. We then took the average of these 10 polarizations to represent the central value in that bin.

To quantify the spread introduced by momentum smearing, we used the maximum and minimum polarization among those 10 samples to set the uncertainty. Thus, each bin's polarization is shown as the mean across the sampled values, and the difference between the highest and lowest sample results provides the vertical error bar. Although the number of random samples is relatively small, it gives a direct sense of how modest momentum mis-measurements—on the order of $0.25 \text{ GeV}/c$—can affect the polarization outcome in each bin.

4.8 Testing the Calculation and Momentum Dependence of Virtual Photon Polarization

4.8.1 Muon Pair Production Rate

This subsection presents the calculated production rates $R_\perp$ and $R_\parallel$ for muon pairs under the setup described earlier. Fig. 23 shows both $R_\perp$ as well as the differences observed between them. Additionally, characteristic fluctuations arising from discrete Landau levels in the presence of a strong magnetic field are also displayed. These fluctuations manifest as dips in specific momentum regions.

In addition to these dips, there is a clear difference in magnitude between $R_\perp$ and $R_\parallel$ at various momenta. This discrepancy reflects the orientation dependence of the production rate relative to the magnetic field: transverse and longitudinal modes behave differently due to Landau-level thresholds and the virtual photon polarization state.

These dips can be interpreted as follows. In a sufficiently strong magnetic field, the internal loop of the virtual photon can "open" at specific energies, al-

lowing for lepton-pair production via Landau-level thresholds. This means the
system finds additional phase-space channels where lepton pairs can form, effec-
tively reducing the production rate in other channels. In this work, we consider
the specific channel where a virtual photon transforms into a lepton pair, then
recombines back into a virtual photon, and finally decays into a real lepton pair.
Where the production rate does not dip (i.e., remains unsuppressed) is the main
contributor to the measurable muon-pair signal. Conversely, the dips indicate
energies at which the strong magnetic field opens new pair-production channels,
redistributing the production strength.

(a) $|eB_y|/m_\pi^2 = 80.5$ (b) $|eB_y|/m_\pi^2 = 63.2$ (c) $|eB_y|/m_\pi^2 = 51.8$

(d) $|eB_y|/m_\pi^2 = 43.6$ (e) $|eB_y|/m_\pi^2 = 37.7$ (f) $|eB_y|/m_\pi^2 = 33.1$

(g) $|eB_y|/m_\pi^2 = 29.3$ (h) $|eB_y|/m_\pi^2 = 26.4$ (i) $|eB_y|/m_\pi^2 = 24.0$

(j) $|eB_y|/m_\pi^2 = 21.9$ (k) $|eB_y|/m_\pi^2 = 20.2$
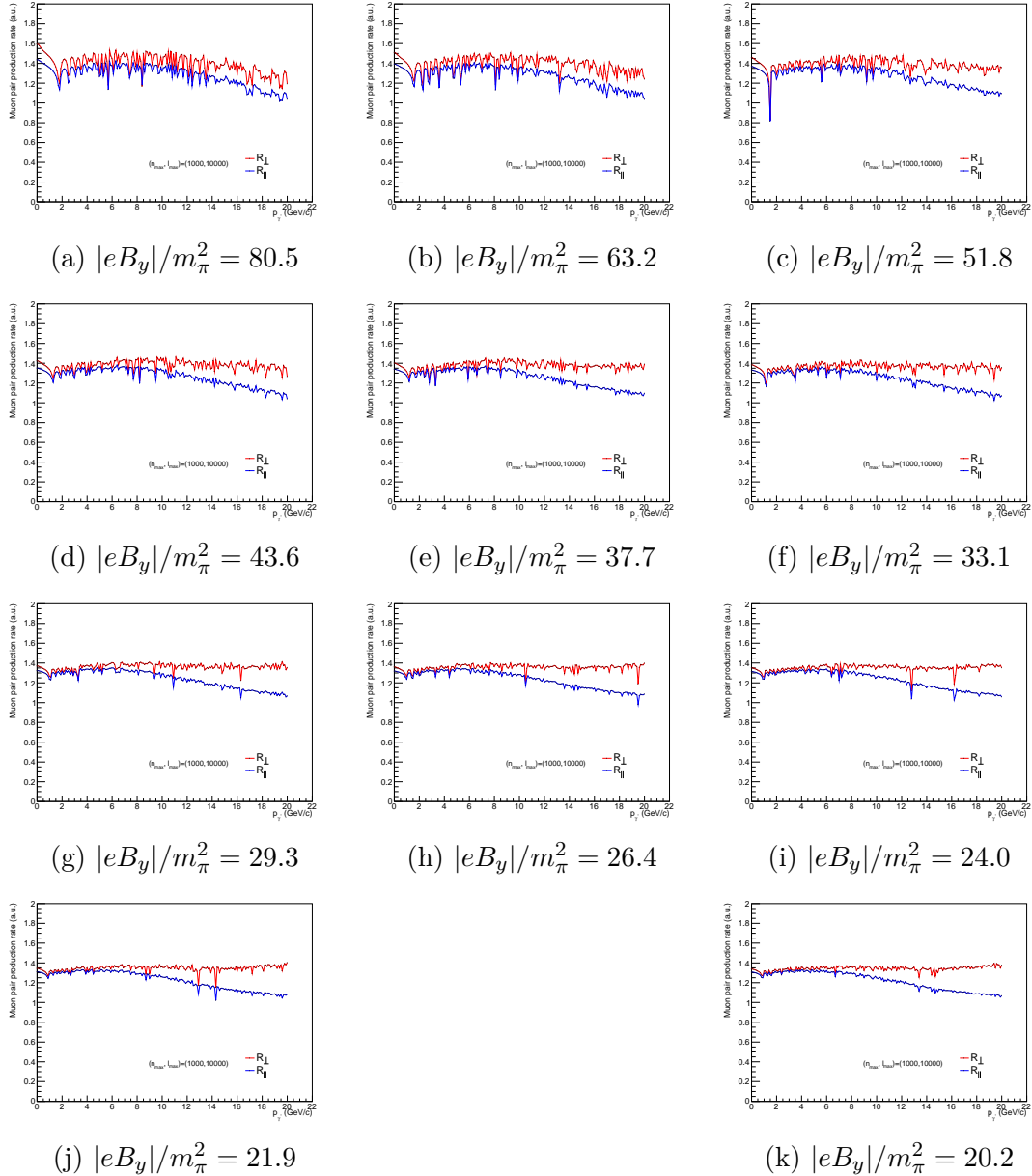
Figure 23: Production rate of muon pair decayed parallel or perpendicular to the
magnetic field direction at each time step for $0.2 < \tau < 0.7\text{fm}/c$

4.9   Dependence of virtual photon momentum

The behavior of virtual photon polarization, P_{cal}, was evaluated using the calculated magnetic field intensity at various time steps. Fig. 24 shows the dependence of P_{cal} on the virtual photon's three-momentum magnitude, $|\mathbf{q}|$, for a magnetic field intensity range $20 < |eB_y|/m_\pi^2 < 80$.

The systematic uncertainties in these calculations originate from two main sources:

- **Momentum resolution:** Fluctuations due to the experimental uncertainty in the virtual photon momentum measurement.

- **Vacuum polarization effects:** Discontinuities and spikes near the threshold where the imaginary component of the vacuum polarization tensor emerges, as predicted in Ref. [39].

The threshold, given by Eq. 4.25, marks a region of rapid change in the calculated polarization, which is particularly sensitive to the intensity of the magnetic field.

The results in Fig. 24 indicate that P_{cal} increases with $|\mathbf{q}|$ for all magnetic field intensities. This trend suggests that measurements at higher momenta are advantageous, as they provide clearer signals with a dominant contribution from prompt photons for $p_{\text{T}} > 4\,\text{GeV}/c$.

4.10   Dependence of intensity of the magnetic field

Figure 25 presents the dependence of P_{cal} on the magnetic field intensity at different time steps, corresponding to momenta in the range $1 < |\mathbf{q}| < 20\,\text{GeV}/c$. Notably, for $13 < |\mathbf{q}| < 20\,\text{GeV}/c$, P_{cal} decreases with increasing magnetic field intensity. This trend highlights the sensitivity of P_{cal} to the time evolution of the magnetic field, as higher field intensities correspond to earlier collision times.

Together, these results underscore the importance of tracking the magnetic field's evolution over time. If the field is still relatively strong when a muon pair is produced, that pair's polarization may be affected more than if the field has already begun to decay. Consequently, interpreting measured muon-pair polarization requires careful consideration of the field's intensity profile throughout the collision.

4.11   Threshold Effects in Form Factors

To understand the dependence on magnetic field intensity, the form factor components (N_0, N_1, and N_2) were analyzed, as shown in Fig. 26. A notable feature is the appearance of thresholds, which are sensitive to the magnetic field intensity. The width of these thresholds increases with stronger magnetic fields, indicating that higher field strengths can influence production rates at different momentum ranges.

For instance, in weaker fields ($|eB_y|/m_\pi^2 \approx 20$), the behavior observed at low momenta ($p_{\gamma^*} \approx 4\,\text{GeV}/c$) reappears at higher momenta ($p_{\gamma^*} \approx 10\,\text{GeV}/c$) for

(a) $|eB_y|/m_\pi^2 = 80.5$

(b) $|eB_y|/m_\pi^2 = 63.2$

(c) $|eB_y|/m_\pi^2 = 51.8$

(d) $|eB_y|/m_\pi^2 = 43.6$

(e) $|eB_y|/m_\pi^2 = 37.7$

(f) $|eB_y|/m_\pi^2 = 33.1$

(g) $|eB_y|/m_\pi^2 = 29.3$

(h) $|eB_y|/m_\pi^2 = 26.4$

(i) $|eB_y|/m_\pi^2 = 24.0$

(j) $|eB_y|/m_\pi^2 = 21.9$

(k) $|eB_y|/m_\pi^2 = 20.2$
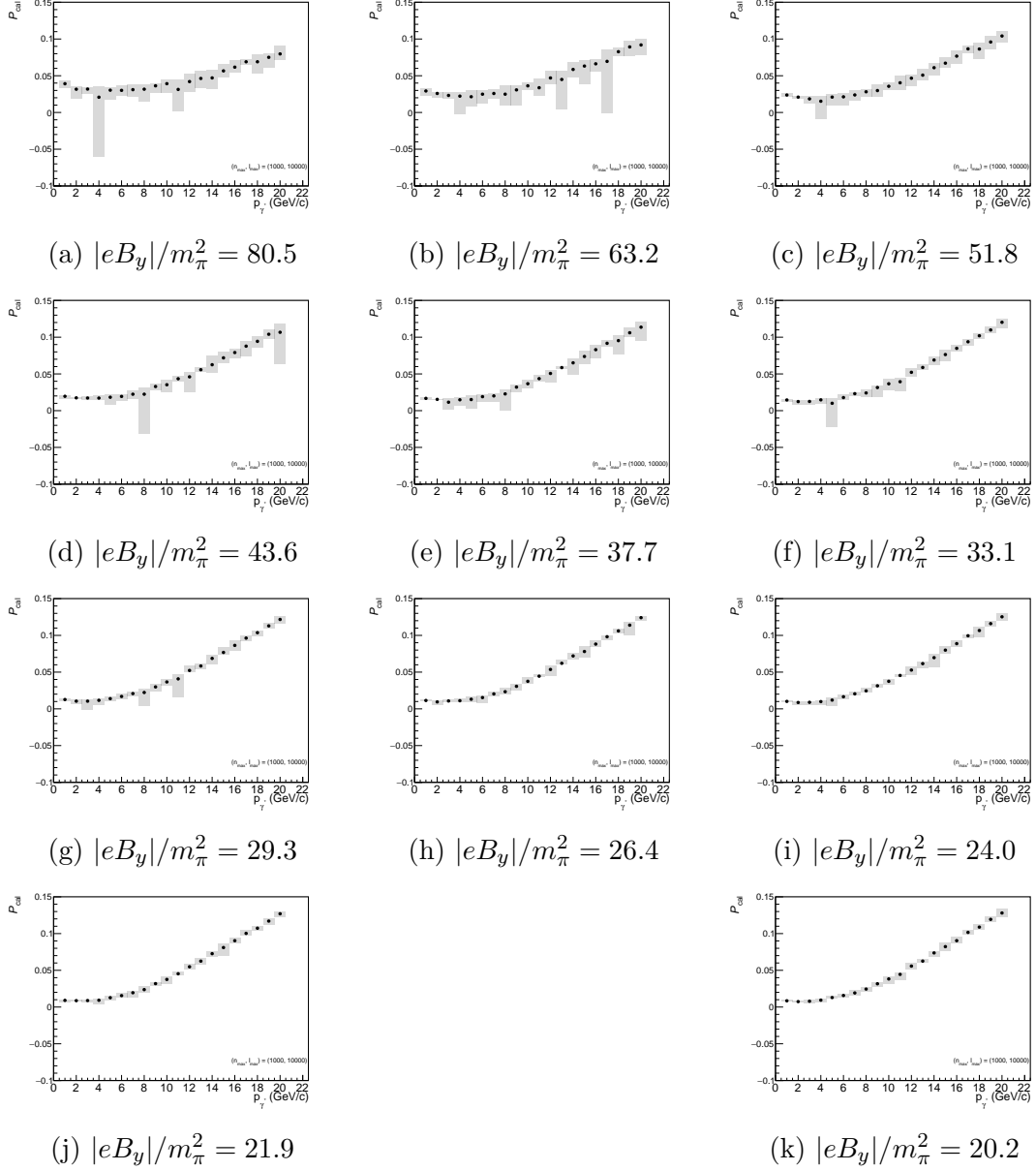
Figure 24: The virtual photon momentum dependence of the virtual photon polarization for $0.2 < \tau < 0.7 \mathrm{fm}/c$
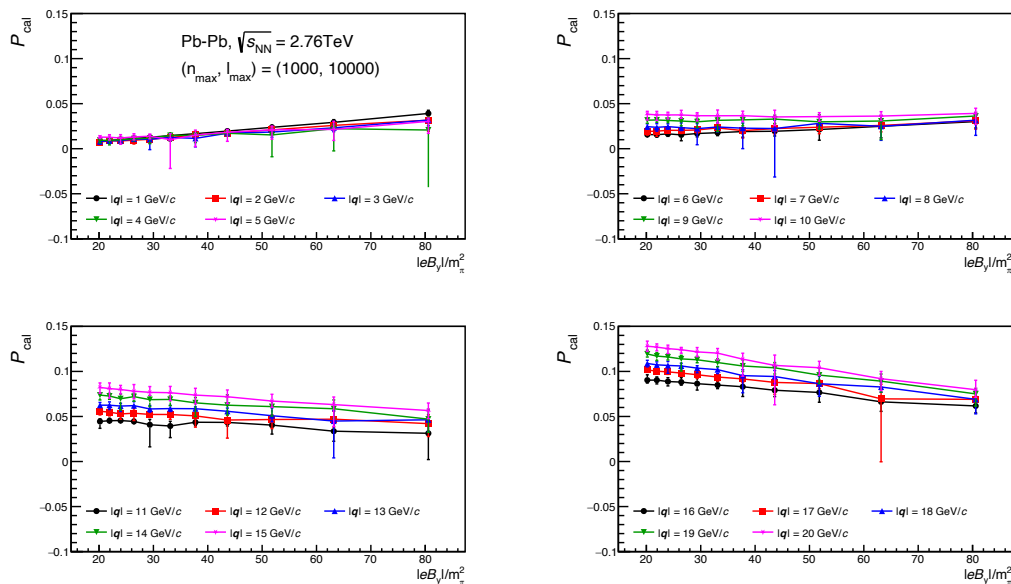
Figure 25: The magnetic field intensity dependence of the virtual photon polarization in the momentum range $1 < |\mathbf{q}| < 20$ GeV/c and the time range $20 < |eB_y|/m_\pi^2 < 80$ in Pb-Pb collisions at $\sqrt{s_{\mathrm{NN}}} = 2.76$ TeV. The calculations were performed using the magnetic field intensity at each time step from Fig. 18. This means that a stronger magnetic field corresponds to an earlier time for the virtual photon polarization.

stronger fields. This suggests that similar underlying physical mechanisms may govern the production rate behavior across different field intensities.

To explore the role of the magnetic field intensity in more detail, we studied the form factor components N_0, N_1, and N_2, as shown in Fig. 26. One striking feature is the emergence of threshold-like structures that depend on the strength of the magnetic field. As the field becomes stronger, these thresholds broaden, indicating that higher field intensities can affect production rates over a wider range of momenta.

An illustrative example may be able to provided by comparing weaker fields ($|eB_y|/m_\pi^2 \approx 20$) to stronger fields. Under weaker fields, a certain behavior appears at low momenta (around $p_{\gamma^*} \approx 4\,\mathrm{GeV}/c$), whereas, under stronger fields, the same behavior re-emerges but at higher momenta (about $p_{\gamma^*} \approx 10\,\mathrm{GeV}/c$). A specific signature that is seen at low momentum in a weaker field shifts to higher momentum in a stronger field, reflecting how the magnetic field modifies the available phase space for virtual photon interactions.

4.12 Implications for Future Measurements

The observed shifts in P_{cal} and the threshold behavior of the form factors emphasize the importance of probing higher momenta and stronger magnetic fields to fully capture the dynamics of virtual photon polarization. Further studies at higher momentum ranges could validate the hypothesized relationship between

(a) $|eB_y|/m_\pi^2 = 80.5$

(b) $|eB_y|/m_\pi^2 = 63.2$

(c) $|eB_y|/m_\pi^2 = 51.8$

(d) $|eB_y|/m_\pi^2 = 43.6$

(e) $|eB_y|/m_\pi^2 = 37.7$

(f) $|eB_y|/m_\pi^2 = 33.1$

(g) $|eB_y|/m_\pi^2 = 29.3$

(h) $|eB_y|/m_\pi^2 = 26.4$

(i) $|eB_y|/m_\pi^2 = 24.0$

(j) $|eB_y|/m_\pi^2 = 21.9$

(k) $|eB_y|/m_\pi^2 = 20.2$
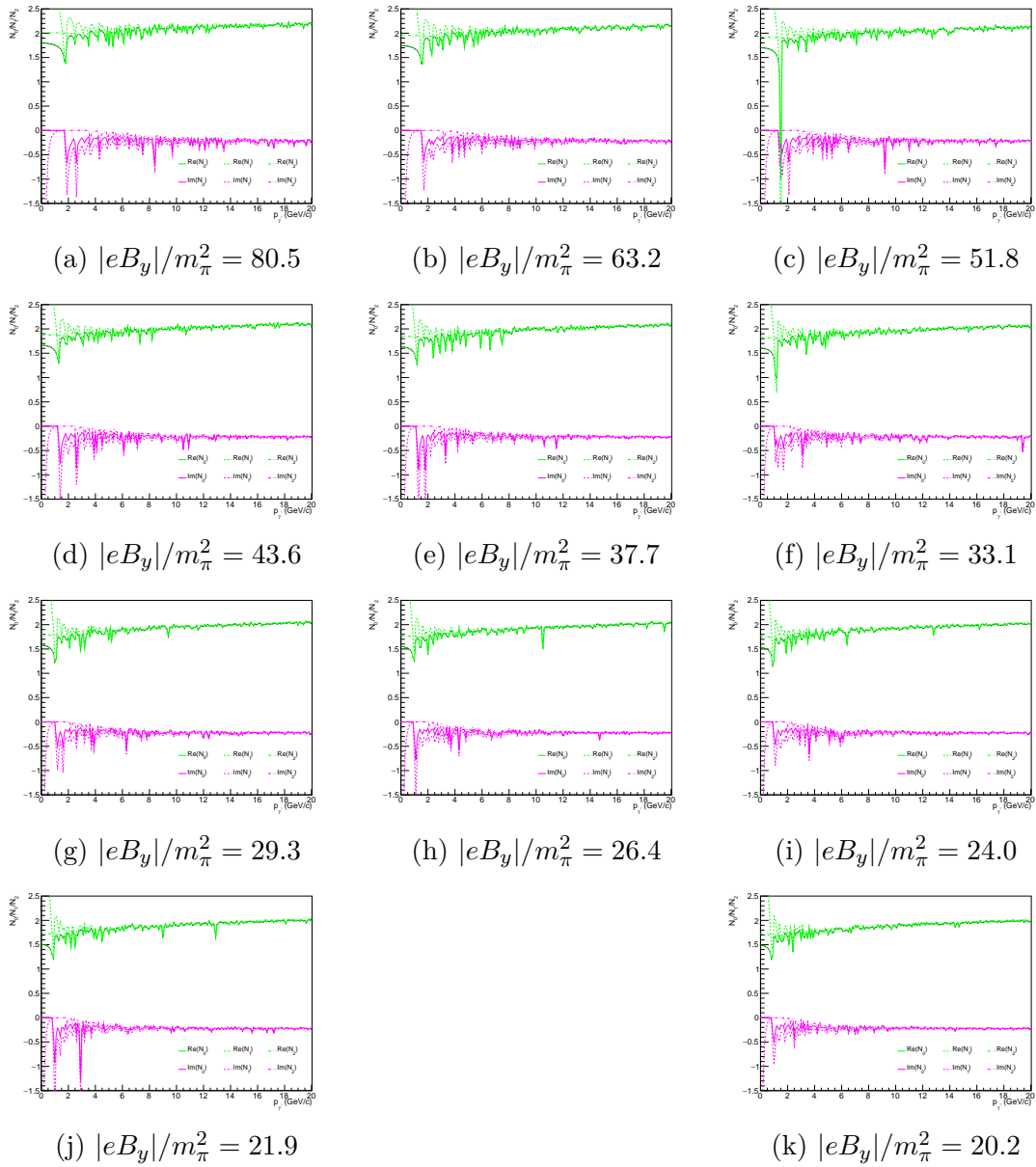
Figure 26: The virtual photon momentum dependence of form factors (N_0, N_1 and N_2) for $0.2 < \tau < 0.7 \mathrm{fm}/c$

low-momentum behaviors in weaker fields and high-momentum effects in stronger fields. Such measurements would enhance our understanding of vacuum polarization and its role in high-energy nuclear collisions.

4.13   Estimation of Virtual Photon Polarization and Feasibility for Pb–Pb Collisions at $\sqrt{s_{\mathrm{NN}}} = 2.76$ TeV

We have estimated the virtual photon polarization, P_{cal}, and evaluated the feasibility of measuring it in Pb–Pb collisions at $\sqrt{s_{\mathrm{NN}}} = 2.76$ TeV, as conducted by the ALICE collaboration. This study focuses on detecting muon pairs originating from the decays of prompt virtual photons produced during the early, high-temperature phase of the collision.

4.13.1   Averaged Virtual Photon Polarization

To assess the polarization expected in the ALICE detector, we take the following steps:

1. We consider magnetic field intensities in the range $20 < |eB_y|/m_\pi^2 < 80$ (see Figs. 18 and 25) for each value of the virtual photon momentum $|\mathbf{q}|$.

2. We then average P_{cal} over $|\mathbf{q}|$ by incorporating the virtual photon production rate. This rate is derived from the Kroll-Wada formula [44], which links the production of real photons to muon pairs via virtual photons, and from a pQCD-based calculation of prompt real-photon yields [51].

3. The integration range in $|\mathbf{q}|$ is $1 < |\mathbf{q}| < 20\,\mathrm{GeV}/c$, chosen to reflect the detector acceptance. The link between total momentum and transverse momentum p_T of the muon pair is given in Eq. 3, implying an approximate range of $0.1 < p_T < 2\,\mathrm{GeV}/c$ for the ALICE muon spectrometer acceptance ($-4.0 < \eta < -2.5$).

$$p = p_{\mathrm{T}} \cosh \eta$$

From these calculations, we obtain

$$\langle P_{\mathrm{cal}} \rangle \; = \; 0.05, \tag{4.30}$$

which serves as a lower bound on the overall polarization. Since P_{cal} increases with $|\mathbf{q}|$ (Fig. 24), extending the momentum range could raise the average polarization. However, due to limitations in the Landau-level summation formula for the virtual photon propagator at large $|\mathbf{q}|$, we conservatively take $\langle P_{\mathrm{cal}} \rangle = 0.05$. In the p_T region above 4 GeV/c, where prompt photons dominate as the signal, the virtual photon polarization increases with total momentum of virtual photon, making 0.05 the lower bound.

4.13.2 Evaluation of Significance at LHC Energies

We next estimate how feasible it would be to detect a photon polarization of $\langle P_{\mathrm{cal}} \rangle = 0.05$ under ALICE conditions at $\sqrt{s_{\mathrm{NN}}} = 2.76$ TeV. Experimentally, prompt-photon processes dominate over decay photons when $p_{\mathrm{T}} > 4$ GeV/c [51], so focusing on muon pairs in this transverse momentum region is reasonable.

Even though Eq. (4.30) was determined in the range $0.1 < p_{\mathrm{T}} < 2$ GeV/c, we apply $\langle P_{\mathrm{cal}} \rangle = 0.05$ to muon pairs with $p_{\mathrm{T}} > 4$ GeV/c. The statistical significance, σ, for detecting a nonzero polarization is defined as:

$$\sigma = \frac{P_{\mathrm{meas}}}{\Delta P_{\mathrm{meas}}}, \tag{4.31}$$

where P_{meas} is the measured photon polarization and ΔP_{meas} its statistical uncertainty. The measured polarization P_{meas} includes contributions from both signal muon pairs arising from prompt virtual photons ($\gamma^* \to \mu\mu$) and background muon pairs:

$$P_{\mathrm{meas}} = \frac{N_\perp - N_\parallel}{N_\perp + N_\parallel}, \tag{4.32}$$

$$N_\perp = \frac{N_{\mathrm{BG}}}{2} + \frac{1 + \langle P_{\mathrm{cal}} \rangle}{2} N_{\mathrm{S}}, \tag{4.33}$$

$$N_\parallel = \frac{N_{\mathrm{BG}}}{2} + \frac{1 - \langle P_{\mathrm{cal}} \rangle}{2} N_{\mathrm{S}}, \tag{4.34}$$

$$\Delta P_{\mathrm{meas}} = \frac{2}{N_\perp + N_\parallel} \sqrt{\frac{N_\perp N_\parallel}{N_\perp + N_\parallel}}, \tag{4.35}$$

where $\langle P_{\mathrm{cal}} \rangle = 0.05$, N_{S} denotes the number of signal events, and N_{BG} denotes the background events. The signal yield N_{S} is estimated by simulating pp collisions in PYTHIA 8 [15, 54] and scaling up to the Pb–Pb dataset collected between 2010 and 2011 [52], while N_{BG} is determined by simulating Pb–Pb collisions in PYTHIA 8 [16] and counting combinatorial muon pairs from random pairing. In this estimation, I used the following scale factors:

$$F_{\mathrm{signal}} = N_{\mathrm{coll}} \frac{\text{statistics in each period with ALICE}}{\#(\text{generated MB events in pp collisions})} \times \frac{20\%}{100\%}$$

$$F_{\mathrm{BG}} = \frac{\text{statistics in each period with ALICE}}{\#(\text{generated MB events in Pb–Pb collisions with centrality } 40\text{--}60\%)} \tag{4.36}$$

where

Using this approach for the 2010–2011 ALICE data at $\sqrt{s_{\mathrm{NN}}} = 2.76$ TeV yields a significance of $0.07\,\sigma$. With the 2015–2018 dataset at $\sqrt{s_{\mathrm{NN}}} = 5.02$ TeV, whose statistics are roughly 5 times higher, the significance improves to $0.15\,\sigma$ for $\langle P_{\mathrm{cal}} \rangle = 0.05$. Although these values are modest, future runs promise higher statistics.

The ongoing Pb–Pb collision experiments at $\sqrt{s_{\mathrm{NN}}} = 5.36$ TeV (planned from 2023 to 2026) will collect up to 100 times the data of earlier runs [52, 5]. This

increase is driven by both an upgraded accelerator―allowing higher collision rates ―and a new continuous data-readout system in the ALICE detector [5]. Under these conditions, our calculations suggest a significance of about $1.7\,\sigma$, assuming $\langle P_{\mathrm{cal}} \rangle = 0.05$.

Although the polarization $\langle P_{\mathrm{cal}} \rangle$ could be higher at $\sqrt{s_{\mathrm{NN}}} = 5.36\,\mathrm{TeV}$ due to a larger Lorentz factor γ and correspondingly stronger magnetic fields [59], we maintain the conservative estimate of $\langle P_{\mathrm{cal}} \rangle = 0.05$. Table 2 summarizes the significance estimates at different energies, highlighting the possibility that future ALICE runs can improve the ability to observe virtual photon polarization and, by extension, probe the intense magnetic fields generated in high-energy heavy-ion collisions.

In $\sqrt{s_{\mathrm{NN}}} = 5.36\,\mathrm{TeV}$, a larger Lorentz factor γ and correspondingly more intense magnetic fields [59] could lead to a higher polarization $\langle P_{\mathrm{cal}} \rangle$. However, we conservatively assume $\langle P_{\mathrm{cal}} \rangle = 0.05$. Table 2 summarizes the estimated significances at various energies, indicating that future ALICE operations can enhance our ability to observe virtual photon polarization and, in turn, explore the intense magnetic fields produced in high-energy heavy-ion collisions.

Moreover, because measurements will be performed at higher p_{T} than those estimated in this study, the true polarization is likely to be larger. In addition, with the newly installed the MFT in ALICE, it becomes possible to remove muons from secondary hadron decays, thereby improving the signal-to-background ratio and further increasing the statistical significance. Nonetheless, we must also be mindful that the effect of the reaction plane resolution―discussed later―could smear the advantage, potentially reducing the gain in significance.

Period	System $\sqrt{s_{\mathrm{NN}}}$	Integrated Luminosity	N_{MB}	Significance
2010–2011	Pb–Pb at 2.76 TeV	75 $\mu\mathrm{b}^{-1}$	1.3×10^8	0.07σ
2015–2018	Pb–Pb at 5.02 TeV	800 $\mu\mathrm{b}^{-1}$	6×10^8	0.15σ
2023–2026	Pb–Pb at 5.36 TeV	13 nb^{-1}	$\sim 10^{10}$	1.7σ

Table 2: Summary of significance estimates at different LHC runs, showing the potential growth in detection feasibility for virtual photon polarization.

These projections underscore that ongoing and upcoming data-taking periods at ALICE may transform virtual photon polarization into a practical probe of the strong magnetic fields present in heavy-ion collisions.

5 Analysis

5.1 Data set in Pb–Pb collisions at $\sqrt{s_{\mathrm{NN}}} = 5.36$ TeV

Minimum-bias events have been analysed in this thesis. The integral luminosity in Pb–Pb collisions at $\sqrt{s_{\mathrm{NN}}} = 5.36\,\mathrm{TeV}$ taken in 2023 was recorded $1535.5\,\mu\mathrm{b}^{-1}$ for Minimum-bias with ALICE shown in 27.
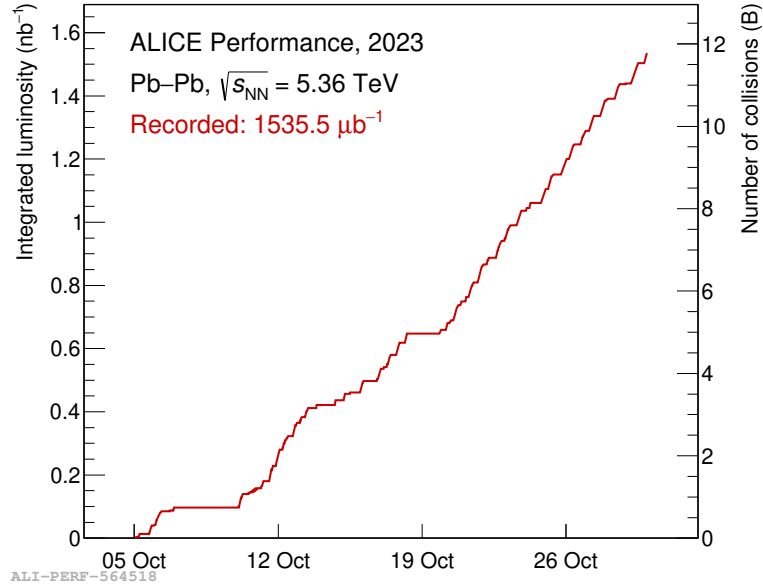
Figure 27: The integrated luminosity in Pb–Pb collisions at $\sqrt{s_{\mathrm{NN}}} = 5.36$ TeV taken in 2023

Run lists

LHC23zzf
544013
LHC23zzg
544028, 544032
LHC23zzh
544091, 544095, 544098, 544116, 544121, 544122, 544123, 544124
LHC23zzi
544184, 544185, 544389, 544390, 544391, 544392
LHC23zzk
544451, 544454, 544474, 544475, 544476, 544477, 544490, 544491, 544492,
544508, 544510, 544511, 544512, 544514, 544515, 554518
LHC23zzl
544548, 544549, 544550, 544551, 544564, 544565, 544567, 544568,
544580, 544582, 544583, 544585
LHC23zzm
544614, 544640, 544652, 544653, 544672, 544674, 544692, 544693,
544694, 544696, 544739, 544742, 544754, 544767
LHC23zzn
544794, 544795, 544797, 544813
LHC23zzo
544868, 544886, 544887, 544896, 544913, 544914, 544917, 544961, 544964,
544968, 544992, 545008, 545009, 545041, 545042, 545044, 545047, 545062,
545063, 545064, 545066, 545117, 545171, 545185, 545210, 545222, 545223,
545246, 545249, 545262, 545291, 545294, 545295, 545296, 545311, 545312,
545332, 545367

5.2   Event selection

Events are selected according to the `eventStandardSel8NoTFBorder` flag, which applies the following requirements:

- Primary Vertex Position: The vertex must lie within ± 10 cm of the nominal interaction point (along the beam axis).

- T0-Vertex Signal (TVX): A valid coincidence between the FT0A and FT0C detectors is required to identify the closest bunch crossing (BC). This ensures a well-defined event timing.

- Time Frame (TF) Borders:

  – The first 300 BCs at the start of the TF and the final 4000 BCs at the end of the TF are excluded.

  – For reference, each TF in 2023–24 runs is 32 orbits long (32×3564 BCs).

- ITS Readout Window:

  – 20 BCs at the end of the ITS readout frame and 10 BCs at the beginning of the frame are also rejected.

  – In Pb–Pb collisions, the ITS readout frame spans about 594 BCs, leading to an approximate 5% loss of events due to this cut.

5.3   Muon selection

To obtain a high-purity muon sample, we apply a series of selection criteria (or "cuts") to each reconstructed muon track. These requirements help remove tracks that might originate from hadronic contamination, secondary interactions, or detector noise, thereby ensuring that the final muon candidates are as clean as possible. The primary selection cuts are:

- *Track type is MCH–MID.* Each track must be reconstructed in both the Muon Tracking Chambers (MCH) and the Muon Identifier (MID). This condition ensures that only fully reconstructed muon trajectories are retained.

- *Pseudorapidity range: $-4 < \eta < -2.5$.* This range focuses on the central portion of the muon spectrometer, excluding tracks lying too close to its edges.

- *Radius at absorber end:* $17.6 < R_{\mathrm{abs}} < 89.5$ cm. Tracks must exit the muon absorber at a distance R_{abs} between 17.6 cm and 89.5 cm from the beam axis. Those outside this range are more likely to be affected by excessive scattering or poorly reconstructed.

- $p \times \mathrm{DCA}$ *cut within* 6σ. Here, p is the muon momentum, and DCA (distance of closest approach) measures how close the extrapolated muon track comes to the collision vertex in the transverse plane. Multiplying p by DCA and imposing a threshold of 6σ rejects tracks that likely did not originate from the primary interaction.

- *Transverse momentum ($p_{\mathrm{T}} > 0.7\,\mathrm{GeV}/c$).* Only muons with p_{T} above $0.7\,\mathrm{GeV}/c$ are accepted, ensuring that the muon can reliably traverse the absorber and be reconstructed with sufficient accuracy.

Once the single-muon selection has been performed, muon candidates are paired into dimuons. Additional criteria applied to these muon pairs include:

- The two muons must have opposite electric charges (i.e., one μ^+ and one μ^-).

- The rapidity of the dimuon must satisfy $2.5 < y < 4.0$, selecting pairs in the forward acceptance of the muon spectrometer.

5.4   Centrality

After applying the event selection criteria, we are obtained approximately 9.4×10^9 accepted collisions. The percentage of collision centrality represents with 0% denoting the most central collisions and 100% the most peripheral collisions. In this analysis, the centrality is estimated using the FT0C detector, as shown in Fig. 28. One observes that the distribution appears relatively flat up to about 80%, indicating that a wide range of collision geometries is well-represented. Notably, the most intense magnetic fields in heavy-ion collisions are expected to occur in the mid-central region, around 40%–60%, where the partial overlap of nuclei can generate large currents but there is still a substantial number of spectator nucleons. This centrality interval is thus of particular interest for studying the maximum effects of the magnetic field.

5.5   Event Plane Determination

In high-energy heavy-ion collisions, the determination of the event-plane angle is essential for determining the direction of the intense magnetic fields. In this analysis, the event-plane angle is reconstructed using the FT0A detector. The calculation employs Q-vectors, which capture the collective anisotropy of the particle emission in a given harmonic order n:

$$
\begin{aligned}
Q_{x,n} &= \sum_{i=1}^{\mathrm{mult}} w_i \cos(n\,\phi_i), \\
Q_{y,n} &= \sum_{i=1}^{\mathrm{mult}} w_i \sin(n\,\phi_i),
\end{aligned}
\tag{5.1}
$$
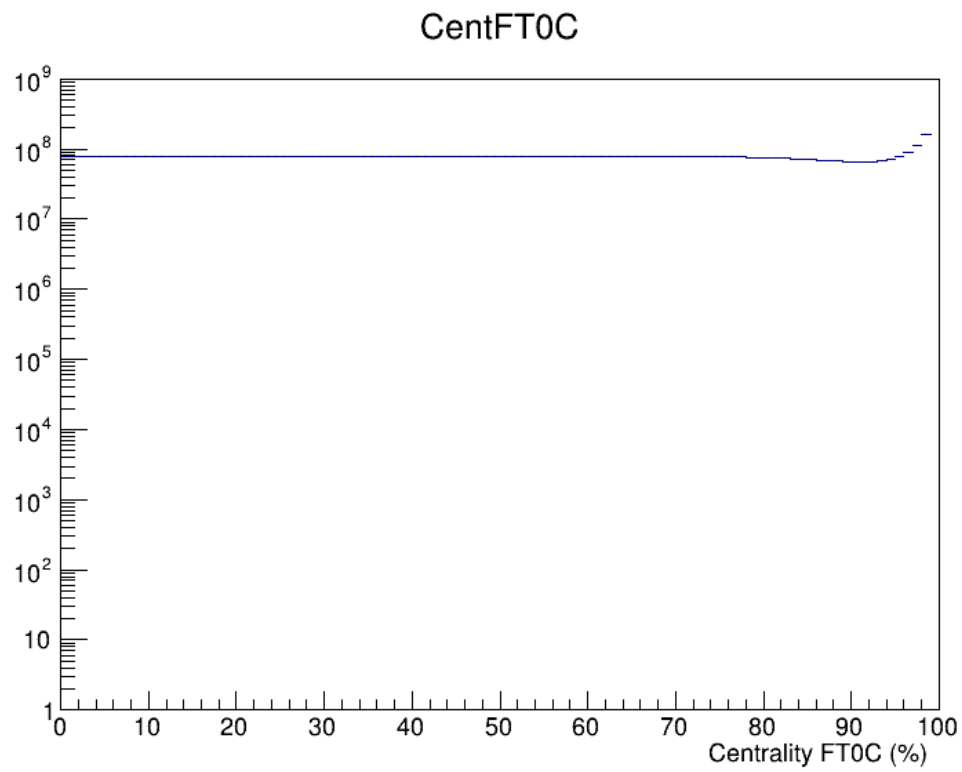
Figure 28: Centrality distribution measured by the FT0C detector.
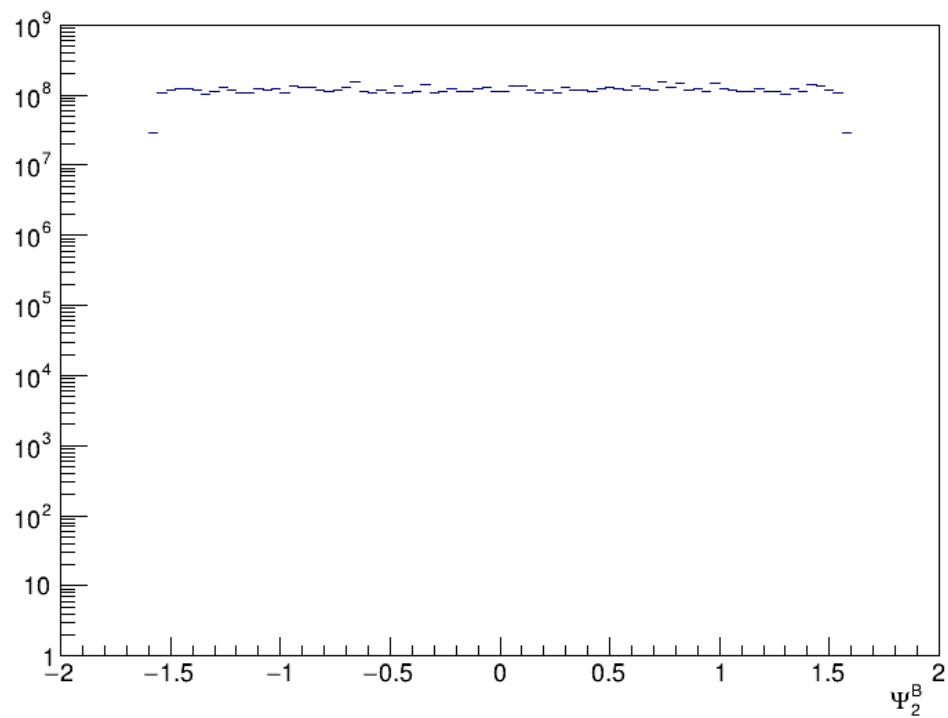
Figure 29: Example distribution of an event-plane angle ψ_2.

where w_i is a calibration weight, and ϕ_i is the azimuthal angle of the i-th particle or detector cell. From these components, the event-plane angle ψ_n is calculated as:

$$\psi_n = \frac{1}{n}\arctan\left(\frac{Q_{y,n}}{Q_{x,n}}\right). \tag{5.2}$$

5.6   Gain Calibration and Q-Vector Correction

Accurate reconstruction of the event-plane angle relies on precise calibration and correction of the Q-vector. This section details the procedures for gain calibration and Q-vector correction, ensuring that the analysis is free from systematic biases.

5.6.1   Gain Calibration

The detector amplitude, representing the number of charged particles traversing a detector channel, is used as a weight in Q-vector calculations. However, variations in gain across different detector channels can introduce systematic biases. To mitigate this, a gain equalization procedure is applied.

For each run, the average amplitude across all channels, $\langle M \rangle$, is calculated. Similarly, the average amplitude for each individual channel i, denoted as $\langle M_i \rangle$, is computed. The corrected amplitude for each channel, M_{cor}, is then obtained using the following formula:

$$M_{\text{cor}} = M_i \times \frac{\langle M \rangle}{\langle M_i \rangle}.$$

This normalization ensures uniform response across all detector channels, improving the reliability of subsequent Q-vector calculations.

5.6.2   Q-Vector Correction

The Q-vector correction addresses geometric and amplitude distortions in the Q-vector distributions. It is performed in three steps: Recentering, Twisting, and Rescaling. Each step removes specific types of distortions, ensuring that the Q-vector accurately reflects the underlying anisotropic flow.

Recentering

The Recentering step shifts the Q-vector distribution to ensure that its average position aligns with the origin. The constants for this correction are:

$$c_1 = \langle Q_{n,x} \rangle, \quad c_2 = \langle Q_{n,y} \rangle,$$

where $Q_{n,x}$ and $Q_{n,y}$ are the components of the Q-vector. The corrected Q-vector components are:

$$Q'_{n,x} = Q_{n,x} - c_1, \quad Q'_{n,y} = Q_{n,y} - c_2.$$

Twisting

Twisting corrects for any misalignment between the axes of the Q-vector distribution and the Cartesian coordinate axes. This is achieved by calculating a

parameter b that characterizes the elliptical distortion:

$$b = \frac{\rho \, \delta Q_{n,x} \delta Q_{n,y}}{\sqrt{(\delta Q_{n,x}^2 - \delta Q_{n,y}^2)^2 + 4(\rho \, \delta Q_{n,x} \delta Q_{n,y})^2}},$$

where $\rho = \frac{\mathrm{Cov}(Q_{n,x}, Q_{n,y})}{\delta Q_{n,x} \delta Q_{n,y}}$ is the correlation coefficient, and $\delta Q_{n,x}$ and $\delta Q_{n,y}$ are the standard deviations of $Q_{n,x}$ and $Q_{n,y}$, respectively. Using b, the twisting correction constants are:

$$c_3 = \frac{b}{\sqrt{\delta Q_{n,x}^2 - b^2}}, \quad c_4 = \frac{b}{\sqrt{\delta Q_{n,y}^2 - b^2}}.$$

The corrected Q-vector components after twisting are:

$$Q_{n,x}'' = \frac{Q_{n,x}' - c_4 Q_{n,y}'}{1 - c_3 c_4}, \quad Q_{n,y}'' = \frac{Q_{n,y}' - c_3 Q_{n,x}'}{1 - c_3 c_4}.$$

Rescaling

Rescaling normalizes the magnitudes of the Q-vector components along both axes to unity. The rescaling constants are:

$$c_5 = \sqrt{\delta Q_{n,x}^2 - b^2}, \quad c_6 = \sqrt{\delta Q_{n,y}^2 - b^2}.$$

The final corrected Q-vector components are:

$$Q_{n,x}''' = \frac{Q_{n,x}''}{c_5}, \quad Q_{n,y}''' = \frac{Q_{n,y}''}{c_6}.$$

These corrections are performed separately for each centrality class, requiring a total of 48 constants for each subsystem. Figures 30 illustrate the step-by-step application of the corrections using a subset of the dataset. After applying all corrections, the event-plane angle distribution appears to be consistent and well-calibrated.

5.6.3   Event-Plane Resolution

The event-plane resolution, R_n^{EP}, quantifies the accuracy of the reconstructed event-plane angle relative to the true event-plane angle, ψ_{true}. Since ψ_{true} is unobservable, the resolution is estimated using a three-subdetector method:

$$R_n^{\mathrm{EP}} = \left\langle \cos\big(n[\psi_A - \psi_{\mathrm{true}}]\big) \right\rangle = \sqrt{\frac{\left\langle \cos\big(n[\psi_A - \psi_C]\big) \right\rangle \left\langle \cos\big(n[\psi_A - \psi_B]\big) \right\rangle}{\left\langle \cos\big(n[\psi_B - \psi_C]\big) \right\rangle}}, \quad (5.3)$$

where ψ_A represent event-plane angle reconstructed by subdetector A (FT0A in this analysis), ψ_B and ψ_C are represent event-plane angles reconstructed by subdetectors B and C (TPC and FT0C, respectively), and n is harmonic order of the Fourier decomposition. In this analysis, $n = 2$ for elliptic flow).

This resolution reflects how well the reconstructed angle ψ_A correlates with the true event-plane angle. The closer R_n^{EP} is to 1, the more accurate the reconstruction.
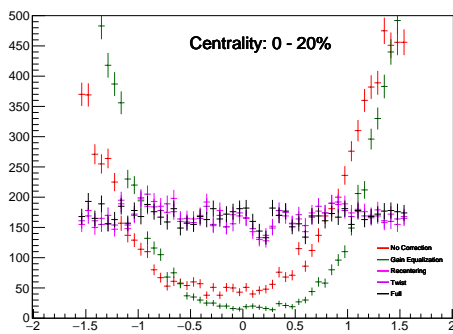
(a) Centrality 0–20%
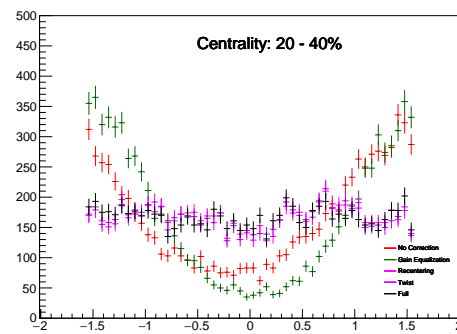
(b) Centrality 20 − 40%
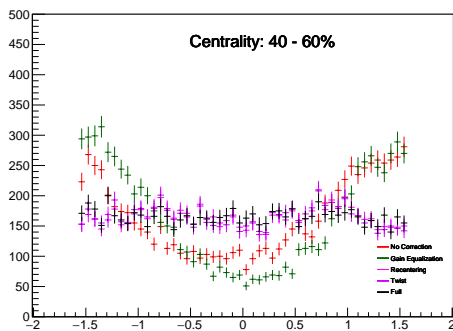
(c) Centrality 40–60%
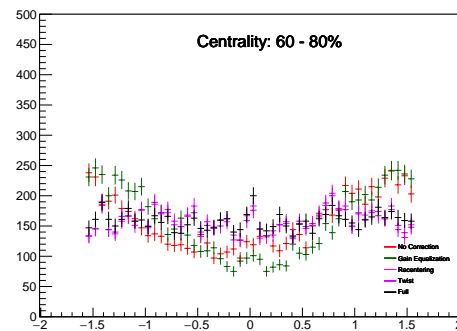
(d) Centrality 60 − 80%

Figure 30: Evolution of Q-vector distributions through correction steps

5.6.4   Using R_n^{EP} to Estimate the Event-Plane Angle Resolution

In this analysis, the event-plane resolution R_n^{EP} (defined in terms of the cosine of the angular difference between the measured and true event-plane angles) is used to approximate the standard deviation, or "resolution," of the event-plane angle. Instead of applying a direct correction to each measured angle, one can estimate the spread in angles, $\Delta\psi_n$, by relating R_n^{EP} to the variance of the difference between the true and reconstructed event-plane angles.

Small-Angle Approximation.   Suppose the event-plane angle is reconstructed as ψ_A while its true value is ψ_{true}. Under the assumption that $\delta\psi = \psi_A - \psi_{\text{true}}$ is small, we can expand:

$$\cos(n\,\delta\psi) \;\approx\; 1 \;-\; \tfrac{1}{2}\left(n\,\delta\psi\right)^2.$$

Since R_n^{EP} is defined as

$$R_n^{\text{EP}} \;=\; \Big\langle \cos\!\big[n\left(\psi_A - \psi_{\text{true}}\right)\big] \Big\rangle,$$

the difference $1 - R_n^{\text{EP}}$ is proportional to the mean square of $(\psi_A - \psi_{\text{true}})$. Solving yields the approximate standard deviation of the angle difference:

$$\Delta\psi_n \;=\; \sqrt{\Big\langle (\psi_A - \psi_{\text{true}})^2 \Big\rangle} \;\approx\; \frac{1}{n}\sqrt{2\left(1 - R_n^{\text{EP}}\right)}. \tag{5.4}$$

This result indicates that R_n^{EP} directly quantifies how sharply (or broadly) the event-plane angle is distributed around its true value. A higher R_n^{EP} (closer to 1) implies a smaller $\Delta\psi_n$ (i.e. better resolution), while a lower R_n^{EP} indicates that the reconstructed angle is more smeared relative to the true angle.

Interpretation in Analyses.   By computing $\Delta\psi_n$ from R_n^{EP}, one gains a concise measure of the event-plane resolution in radians. For instance, in elliptic flow ($n = 2$) analyses, $\Delta\psi_2$ serves as a standard figure of merit when comparing different detectors or collision systems. This measure tells us how reliably ψ_A approximates ψ_{true} on average, which is crucial for flow studies, anisotropy measurements, and any analysis that depends on the orientation of the reaction plane (such as magnetic-field-induced polarization or correlations).

Practical Considerations.

- If $\delta\psi$ becomes large, the small-angle approximation $\cos(n\,\delta\psi) \approx 1 - \tfrac{1}{2}\left[\,n(\delta\psi)\,\right]^2$ no longer holds, and more detailed treatment of the resolution may be needed.

- $\Delta\psi_n$ is an *average* or *RMS* measure of angle smearing across events, not a per-event correction.

- In many heavy-ion experiments (e.g. at RHIC and LHC), the standard usage of Eq. (5.4) is well established, allowing straightforward comparisons of resolution factors across different runs or detector configurations.
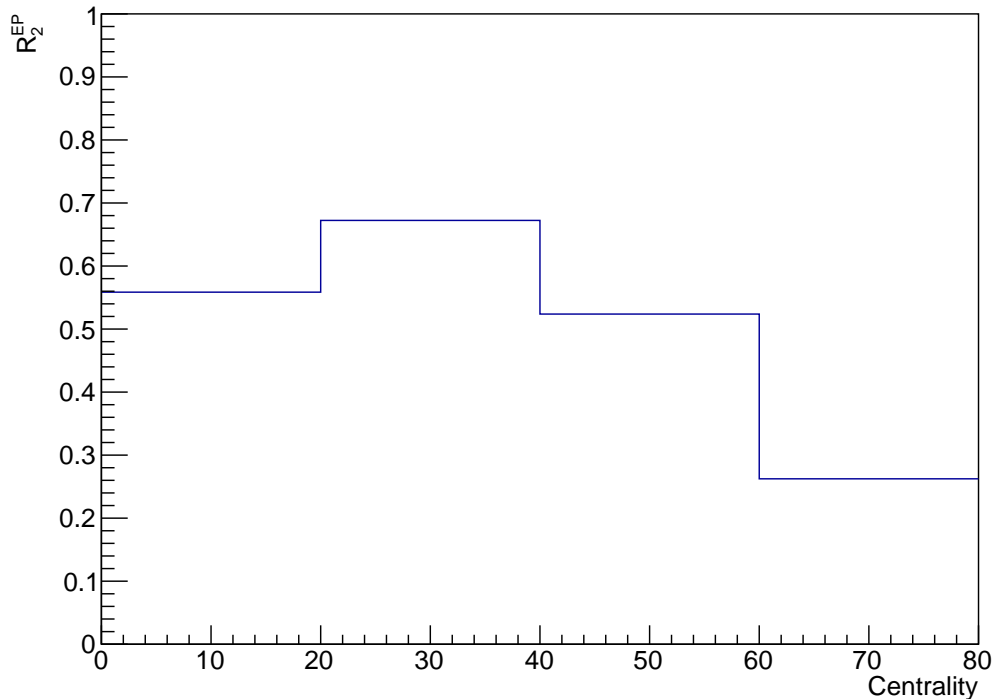
Figure 31: The uncertainty of event plane angle using cosine function with each centrality

In Fig. 31 and Fig. 32, we show how the uncertainty in the event-plane angle varies with collision centrality. Figure 31 displays the resolution factor R_2^{EP}, which decreases in peripheral collisions because, in more peripheral events, the smaller reaction area makes it harder to determine the event plane precisely. Figure 32 then converts that resolution factor into an angular uncertainty using the relation discussed in the previous subsection. These uncertainties provide valuable guidance for choosing bin sizes when performing measurements of virtual photon polarization, as they indicate how finely one can reliably slice the data in angle between the intense magnetic field and muon pair.

6 Results

6.1 Raw Yield Extraction with the Like-Sign Method

The identification of physical signals in heavy-ion collision experiments often requires careful separation of correlated pairs from uncorrelated pairs. A prevalent source of background arises from pairs of particles that do not originate from a common physical process (e.g., virtual photon decay or resonance decay), but rather come from independent production in the collision. To tackle this issue, the like-sign method is commonly employed to estimate and subtract the uncorrelated background component from the observed opposite-sign muon pairs.
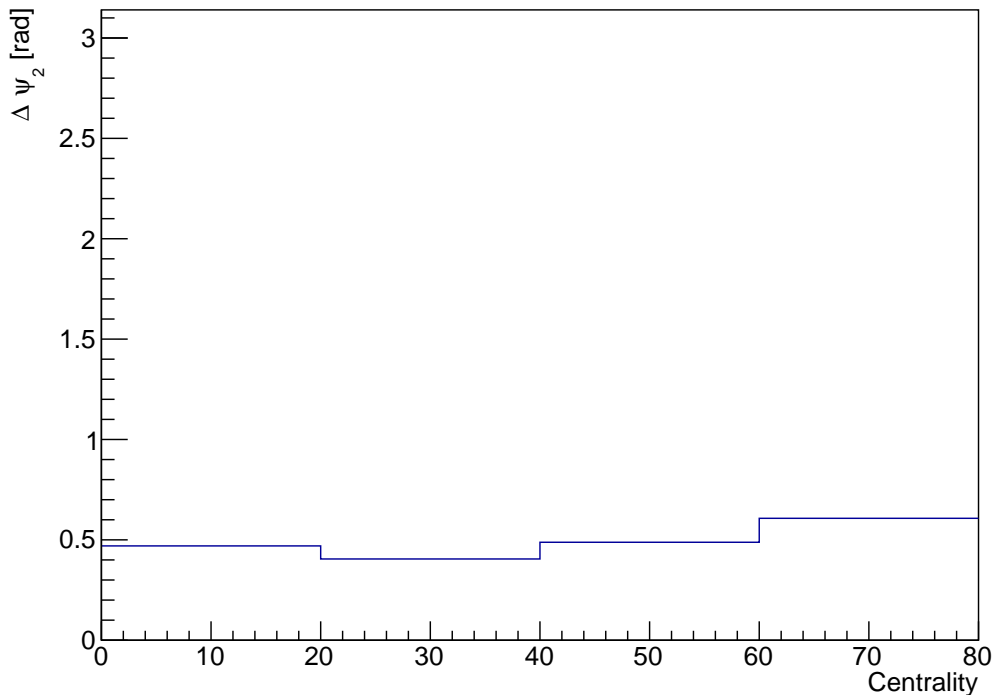
Figure 32: The uncertainty of event plane angle with each centrality

The like-sign method takes advantage of the fact that like-sign muon pairs ($\mu^+\mu^+$ or $\mu^-\mu^-$) are predominantly uncorrelated. By examining the invariant mass (or other kinematic distributions) of these like-sign pairs, one obtains a template for the uncorrelated background present in the opposite-sign sample ($\mu^+\mu^-$).

Specifically, we construct distributions for both like-sign and unlike-sign pairs:

- **Like-sign pairs**: Dominated by accidental, uncorrelated combinations.

- **Unlike-sign pairs**: Contains a mixture of physically correlated signals and uncorrelated background.

By comparing these two types of distributions, one can subtract the combinatorial background from the OS sample and isolate the signal of interest.

Let N_{+-}^{same} represent the observed yield of opposite-sign muon pairs in a given kinematic bin (e.g., invariant mass). This yield consists of two components: a true physical signal S and an uncorrelated background B:

$$N_{+-}^{\text{same}} = S + B. \tag{6.1}$$

The background B is estimated by examining the like-sign yields in the same event, N_{++}^{same} and N_{--}^{same}. Because these like-sign pairs are assumed to be entirely combinatorial, one can approximate:

$$B = 2R \times \sqrt{N_{++}^{\text{same}} \cdot N_{--}^{\text{same}}}. \tag{6.2}$$

Here, the factor of 2 accounts for both charge states, and R is a correction factor that compensates for any detection efficiency differences between positively and negatively charged muons.

The factor R is evaluated using mixed-event distributions, where muons from different events are combined to eliminate genuine correlations. In these mixed events, one computes the yields N_{+-}^{mix}, N_{++}^{mix}, and N_{--}^{mix}. The factor R is then given by:

$$R = \frac{N_{+-}^{\mathrm{mix}}}{2\sqrt{N_{++}^{\mathrm{mix}} \cdot N_{--}^{\mathrm{mix}}}}. \tag{6.3}$$

A value of $R \approx 1$ indicates nearly identical detection efficiencies for positive and negative charges, while $R \neq 1$ implies non-negligible efficiency differences or acceptance asymmetries.

Once B is estimated, the physical signal S is computed by:

$$S = N_{+-}^{\mathrm{same}} - B. \tag{6.4}$$

To assess the reliability of this extracted signal, we define the statistical significance as:

$$\mathrm{Significance} = \frac{S}{\Delta S}, \quad \Delta S = \sqrt{S + 2B}. \tag{6.5}$$

This metric quantifies how clearly the signal stands out relative to the background fluctuations.

Figure 33 shows the observed unlike-sign (OS) pair distribution, the combinatorial background estimated by the like-sign method, and the signal after background subtraction in four centrality classes: 0–20%, 20–40%, 40–60%, and 60–80%. In all classes, one can identify peaks corresponding to η, ω, and ρ mesons once the background has been subtracted.

Figures 34–37 illustrate how the signal-to-background ratio (S/B), the statistical significance, and the R factor vary with collision centrality. These results demonstrate both the effectiveness and the limitations of the like-sign method in isolating physically correlated muon pairs from large combinatorial backgrounds in heavy-ion collision data.

6.2 Angular distribution of muon pairs

An essential ingredient for observing virtual photon polarization is the angle between the muon pair's decay plane and the intense magnetic field. As introduced in Sec. 4.5, we define and measure this angle using reconstructed muon pairs and the event-plane angle.

Figures 38–41 show the decay-plane angle distribution of opposite-sign or like-sign muon pairs in same event (denoted by $\psi_{\mu\mu} - \Psi_{\mathrm{EP}}$) separated into intervals of size $\pi/2$. Here,

- $0 < \psi_{\mu\mu} - \Psi_{\mathrm{EP}} < \pi/4$ and $3\pi/4 < \psi_{\mu\mu} - \Psi_{\mathrm{EP}} < \pi$ represent angles labeled as "parallel" to the strong magnetic field, and

- $\pi/4 < \psi_{\mu\mu} - \Psi_{\mathrm{EP}} < 3\pi/4$ represents angles labeled as "perpendicular" to the field.

(a) Centrality 0–20%

(b) Centrality 20 − 40%

(c) Centrality 40–60%

(d) Centrality 60 − 80%
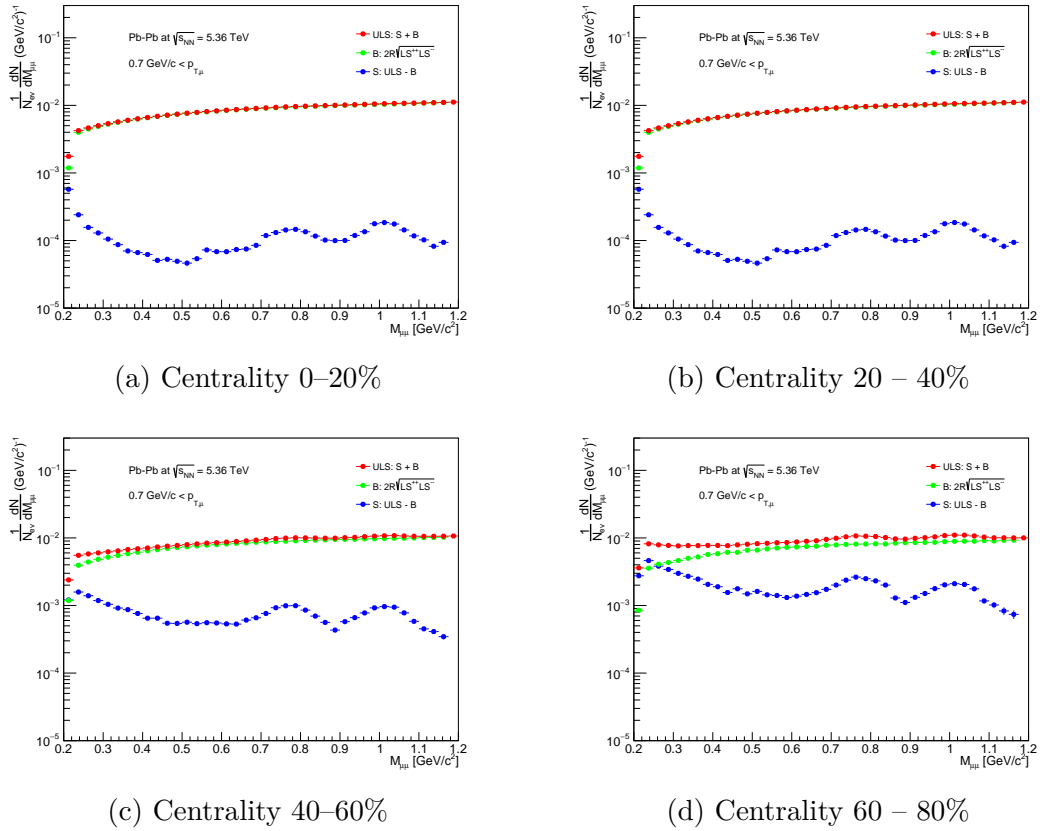
Figure 33: The correlated muon pair extraction in 4 centrality classes

(a) S/B

(b) Significance
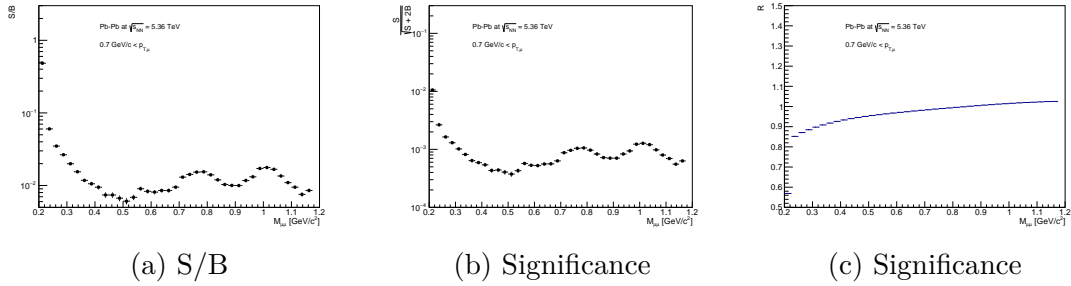
(c) Significance

Figure 34: S/B ,significance and R factor in the 0–20% centrality class

(a) S/B

(b) Significance
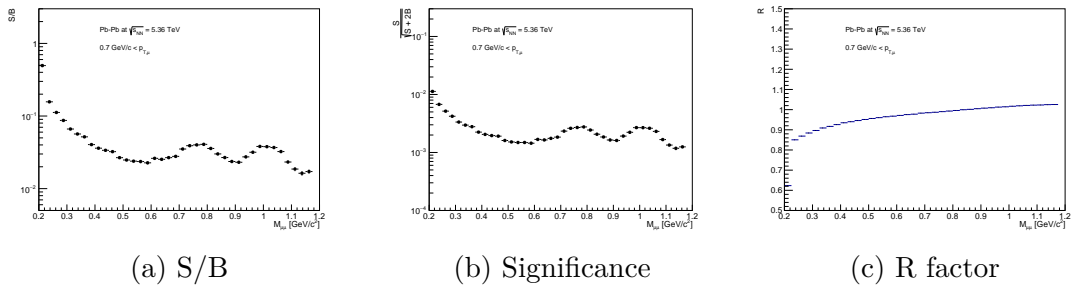
(c) R factor

Figure 35: S/B, significance and R factor in the 20–40% centrality class

(a) S/B

(b) Significance
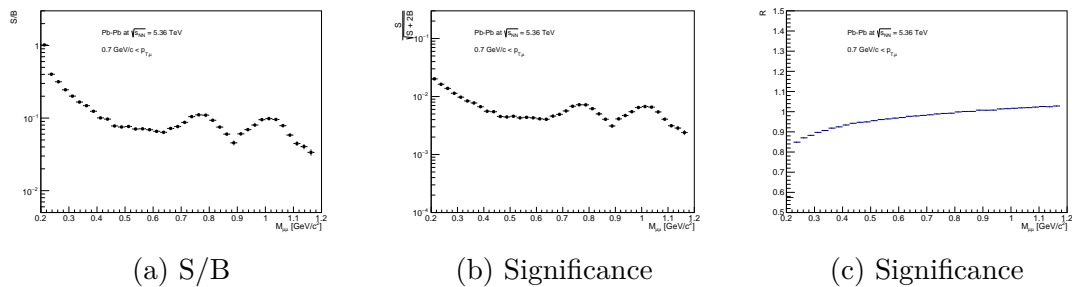
(c) Significance

Figure 36: S/B, significance and R factor in the 40–60% centrality class

(a) S/B

(b) Significance
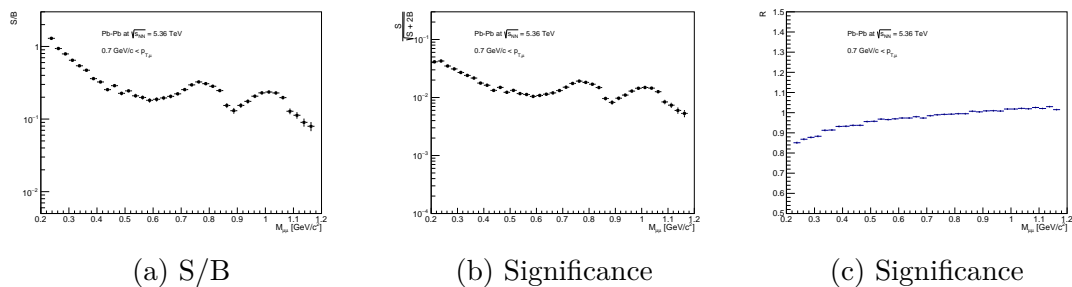
(c) Significance

Figure 37: S/B, significance and R factor in the 60–80% centrality class

With these definitions, we can investigate how the muon pair's decay plane aligns with or is oriented relative to the magnetic field in different bins.

Muon pair decayed from J/ψ have potential polarization to response with the direction of the intense magnetic field [6]. To limit contamination from this source, the analysis is performed in several invariant-mass ranges for the muon pairs: $M_{\mu\mu} < 500$ MeV/c^2, < 700 MeV/c^2, < 1000 MeV/c^2, and < 1200 MeV/c^2. By restricting the mass of the muon pair, we reduce the contributions from hadronic decay channels whose polarization might interfere with the signal from prompt virtual photons.

In all centrality classes studied, the measured angular distributions in these mass bins are consistent with zero as shown in Figs. 42.

Subtraction of Uncorrelated Muon Pairs

In high-energy heavy-ion collisions, not every opposite-sign muon pair ($\mu^+\mu^-$) is formed by a single, physically correlated source. Many such pairs arise by chance from unrelated muons in the same event, referred to as uncorrelated background. To address this issue, we use the like-sign method introduced in the previous section, along with the previously determined R factor, to subtract these uncorrelated contributions from the opposite-sign distribution. By removing this background, the angular distributions of muon pairs can better reflect physically correlated pairs, such as those from prompt virtual photons.

Figure 43 shows the decay-plane angle distribution after subtracting uncorrelated muon pairs via the like-sign method, plotted for different mass and centrality classes. In many of these categories, the measured distribution deviates from
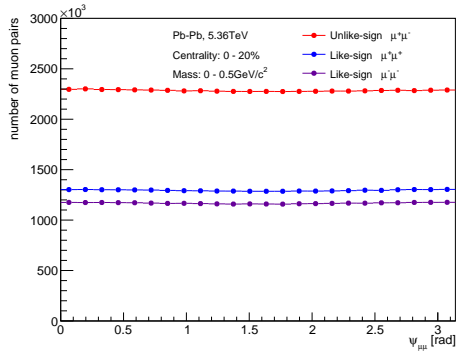
(a) Centrality 0–20%
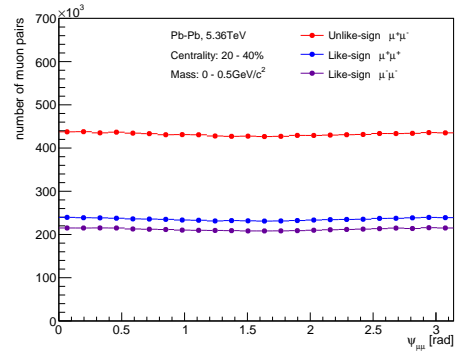
(b) Centrality 20 − 40%
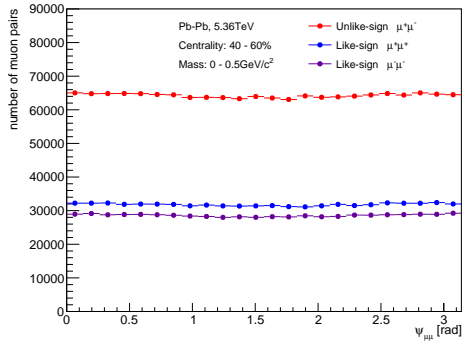
(c) Centrality 40–60%
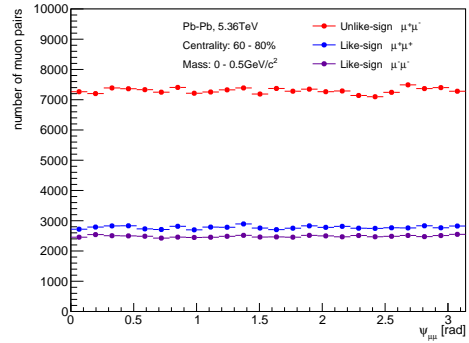
(d) Centrality 60 − 80%

Figure 38: The angle of muon pair's decay plane with opposite-sign and like-sign muon pairs for $0.2 < M_{\mu\mu} < 0.5$ GeV/c^2

(a) Centrality 0–20%

(b) Centrality 20 − 40%

(c) Centrality 40–60%
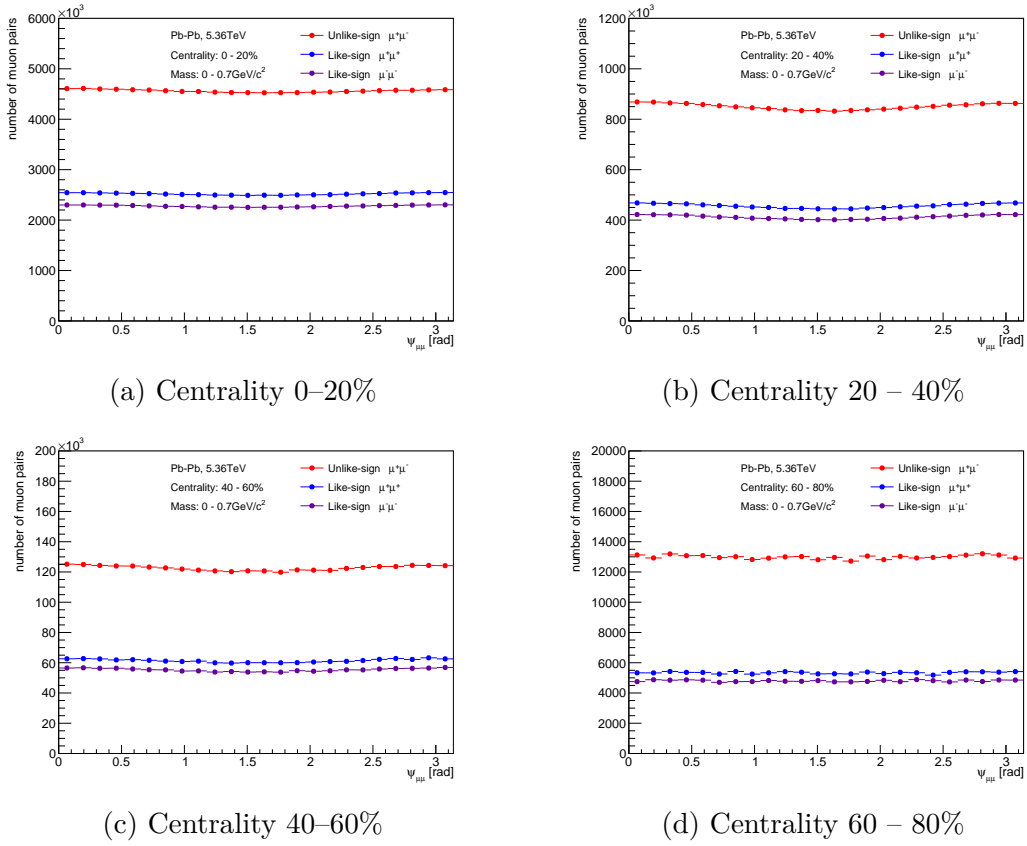
(d) Centrality 60 − 80%

Figure 39: The angle of muon pair's decay plane with opposite-sign and like-sign muon pairs for $0.2 < M_{\mu\mu} < 0.7$ GeV/c^2
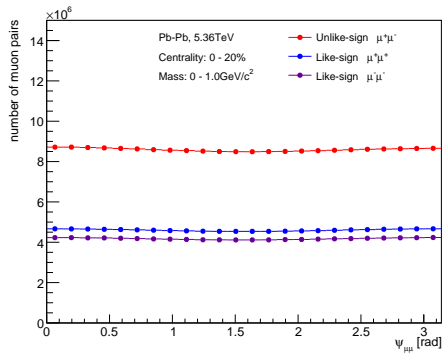
(a) Centrality 0–20%
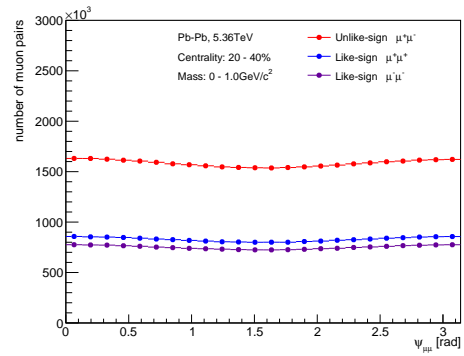
(b) Centrality 20 − 40%
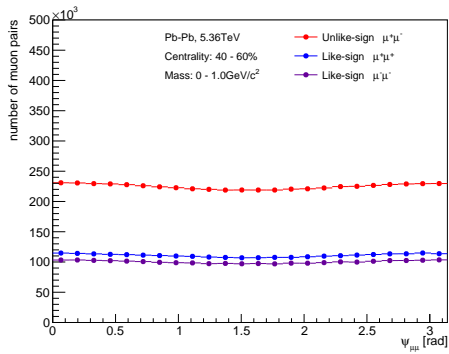
(c) Centrality 40–60%
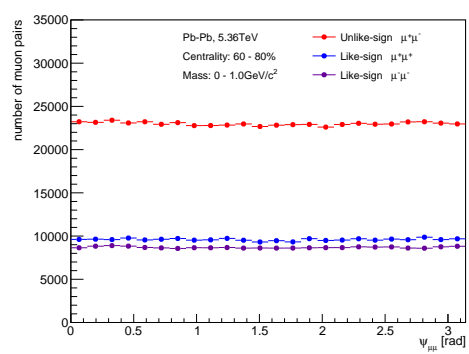
(d) Centrality 60 − 80%

Figure 40: The angle of muon pair's decay plane with opposite-sign and like-sign muon pairs for $0.2 < M_{\mu\mu} < 1.0$ GeV/c^2

(a) Centrality 0–20%

(b) Centrality $20 - 40\%$

(c) Centrality 40–60%

(d) Centrality $60 - 80\%$
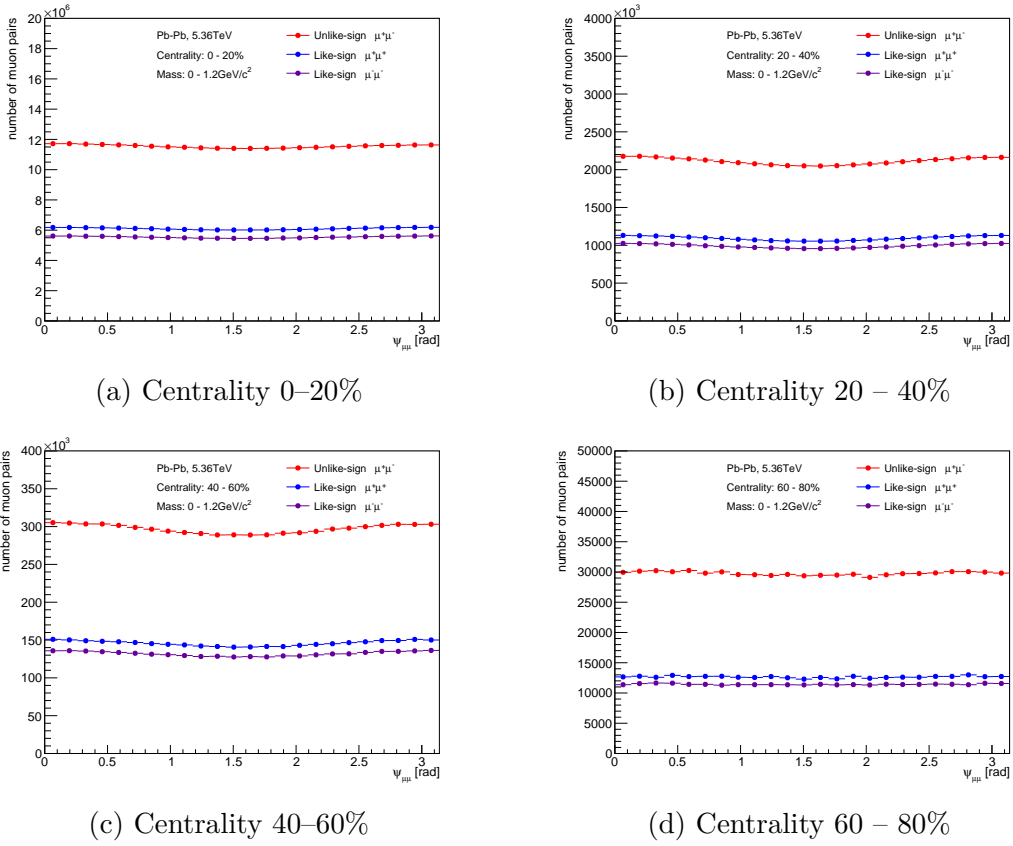
Figure 41: The angle of muon pair's decay plane with opposite-sign and like-sign muon pairs for $0.2 < M_{\mu\mu} < 1.2$ GeV/c^2
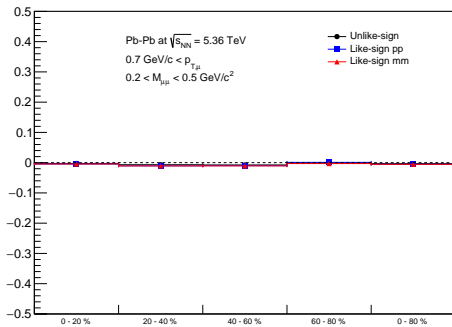
(a) $0.2 < M_{\mu\mu} < 0.5$ GeV/c^2
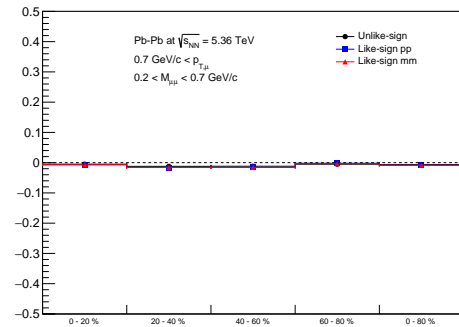
(b) $0.2 < M_{\mu\mu} < 0.7$ GeV/c^2
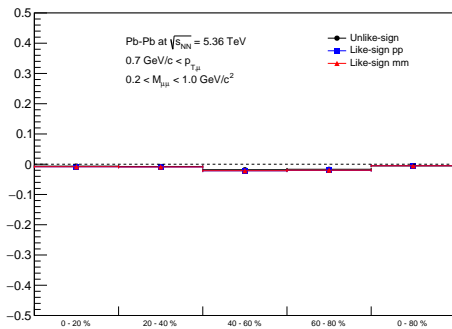
(c) $0.2 < M_{\mu\mu} < 1.0$ GeV/c^2
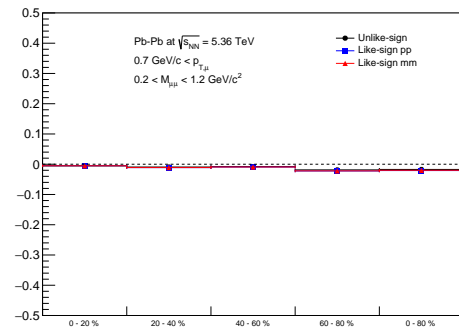
(d) $0.2 < M_{\mu\mu} < 1.2$ GeV/c^2

Figure 42: Polarization of opposite-sign or like-sign muon pairs in the same event with 4 mass classes

zero, suggesting that the muon pairs could be polarized. However, these non-zero values cannot yet be definitively attributed to the intense magnetic field, because additional effects such as elliptic collective flow and jets may also influence the distribution. Nevertheless, the results indicate that muon pairs exhibit possible signs of polarization, motivating further study to disentangle the different physics contributions.

(a) $0.2 < M_{\mu\mu} < 0.5$ GeV/c^2

(b) $0.2 < M_{\mu\mu} < 0.7$ GeV/c^2

(c) $0.2 < M_{\mu\mu} < 1.0$ GeV/c^2

(d) $0.2 < M_{\mu\mu} < 1.2$ GeV/c^2
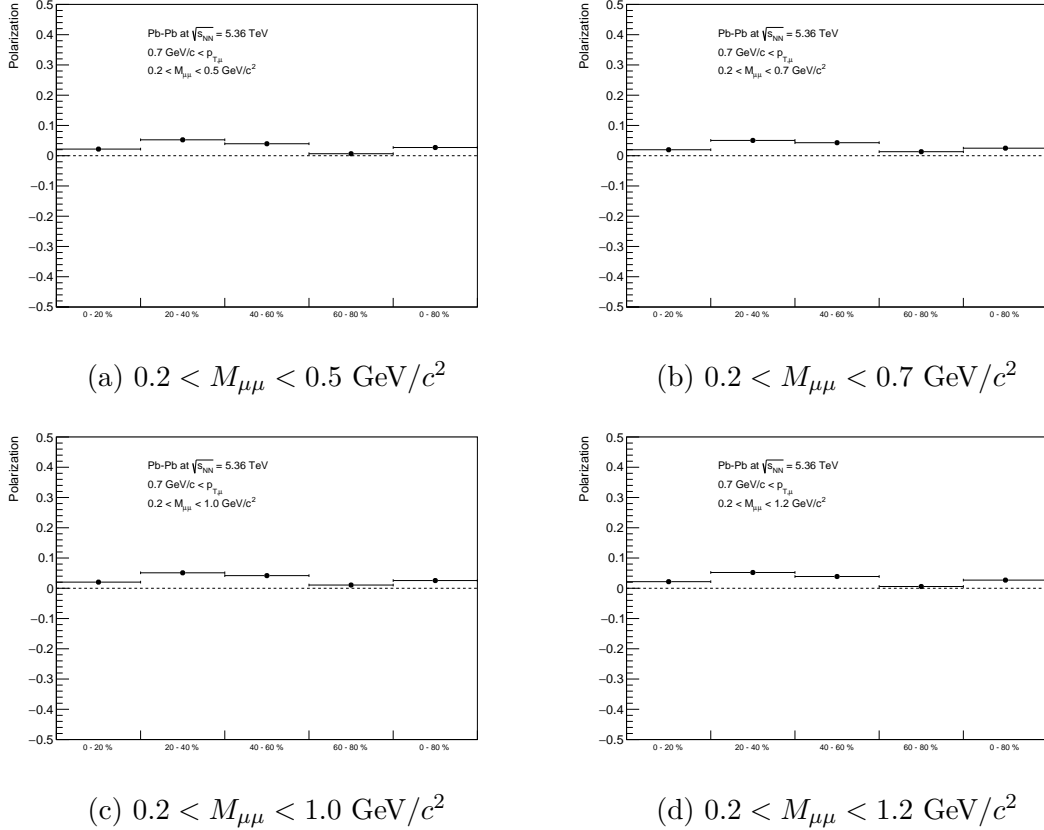
Figure 43: Polarization with 4 mass classes after subtraction of uncorrelated background using like-sign method

7 Conclusion

This dissertation investigates the feasibility of measuring virtual photon polarization in high-energy heavy-ion collisions at the LHC, with a particular focus on muon pairs detected with the ALICE. The motivation arises from theoretical predictions that the intense magnetic fields generated in heavy-ion collisions, potentially surpassing the Schwinger limit, could lead to anisotropic decays of virtual photons into muon pair as one aspect of nonlinear QED. By examining muon pairs, the goal is to detect signs of this polarization and thereby provide a new means of probing the intense magnetic fields and their interaction with the QGP.

One of the main challenges in measuring virtual photon polarization is distinguishing the small polarization signal from the abundant background. Combinatorial muon pairs, as well as decays of hadrons and heavy-flavor mesons, may obscure the prompt virtual photon signal. In this study, we clarify the measurability of virtual photon polarization in Pb – Pb collisions recorded between 2023 and 2026.

A key element of this work involves refining theoretical estimates of polarization in a realistic scenario where the magnetic field evolves over time. Many earlier analyses assumed a static field at its maximum intensity. Here, to incorporate finite electrical conductivity in the QGP and time-dependent magnetic-field decay, we adopt a resistive relativistic magnetohydrodynamics (RRMHD) model. The muon pair production rate was calculated by considering the one-loop vacuum polarization contributions influenced by the magnetic field strength at each time step. Under conditions relevant to ALICE's muon spectrometer, these calculations suggest that the virtual photon polarization could reach $\langle P_{\mathrm{cal}} \rangle \approx 0.05$ in the momentum range $0 < p_{\gamma^*} < 20\,\mathrm{GeV}/c$. The number of signal events and combinatorial background was estimated via simulation and then scaled to match the statistics from each data taking period.

The statistical significance was 0.07σ using the data in Pb–Pb collisions in 2011–2012. Although the data in Pb–Pb collisions collected in 2015–2018 had higher statistics than the previous data, it increased by 0.15σ. It is indicated that limitations due to the currently available data samples. However, ongoing and planned Pb – Pb runs at $\sqrt{s_{\mathrm{NN}}} = 5.36\,\mathrm{TeV}$ will substantially change the situation. Improvements in accelerator luminosities, continuous readout capabilities in ALICE, and an approximately hundredfold increase in the number of recorded events are expected to overcome existing statistical limitations. Under these upgraded conditions, estimates suggest that it could reach about 1.7σ. Although this level is still below a firm discovery threshold, it is markedly more promising than what was achievable with previous datasets.

In analysis of Pb – Pb collision taken in 2023, we combined the like-sign method with careful consideration of event plane resolution to mitigate these effects. Although the existing run data did not yield a statistically significant observation, a key outcome of this study is that virtual photon polarization in ALICE shows promise as a means of exploration.

Overall, this dissertation highlights the potential of measuring virtual photon polarization as a new avenue for studying the intense magnetic fields produced in high-energy heavy-ion collisions. While the current datasets lack sufficient statistical power for a conclusive result, upcoming runs at higher statistics with improved detection and readout capabilities may allow the measurement to reach a detectable level of significance. Such progress would deepen insights into the interplay between QCD matter and intense magnetic fields, further expanding our understanding of high-energy physics.

Acknowledge

References

[1] K. Aamodt et al. "The ALICE experiment at the CERN LHC". In: *JINST* 3 (2008), S08002. DOI: 10.1088/1748-0221/3/08/S08002.

[2] Gert Aarts and Aleksandr Nikolaev. "Electrical conductivity of the quark-gluon plasma: perspective from lattice QCD". In: *The European Physical Journal A* 57.4 (Apr. 2021), p. 118. ISSN: 1434-6001, 1434-601X. DOI: 10.1140/epja/s10050-021-00436-5.

[3] M. I. Abdulhamid et al. "Observation of the Electromagnetic Field Effect via Charge-Dependent Directed Flow in Heavy-Ion Collisions at the Relativistic Heavy Ion Collider". In: *Phys. Rev. X* 14 (1 Feb. 2024), p. 011028. DOI: 10.1103/PhysRevX.14.011028. URL: https://link.aps.org/doi/10.1103/PhysRevX.14.011028.

[4] S. Acharya et al. "ALICE upgrades during the LHC Long Shutdown 2". In: *Journal of Instrumentation* 19.05 (May 2024), P05062. ISSN: 1748-0221. DOI: 10.1088/1748-0221/19/05/p05062. URL: http://dx.doi.org/10.1088/1748-0221/19/05/P05062.

[5] S. Acharya et al. "ALICE upgrades during the LHC Long Shutdown 2". In: *Journal of Instrumentation* 19.05 (May 2024), P05062. ISSN: 1748-0221. DOI: 10.1088/1748-0221/19/05/p05062. URL: http://dx.doi.org/10.1088/1748-0221/19/05/P05062.

[6] S. Acharya et al. "Measurement of the J/ψ Polarization with Respect to the Event Plane in Pb-Pb Collisions at the LHC". In: *Phys. Rev. Lett.* 131 (4 July 2023), p. 042303. DOI: 10.1103/PhysRevLett.131.042303. URL: https://link.aps.org/doi/10.1103/PhysRevLett.131.042303.

[7] S. Acharya et al. "Probing the Effects of Strong Electromagnetic Fields with Charge-Dependent Directed Flow in Pb-Pb Collisions at the LHC". In: *Phys. Rev. Lett.* 125 (2 July 2020), p. 022301. DOI: 10.1103/PhysRevLett.125.022301.

[8] J. Adam et al. "Direct photon production in Pb−Pb collisions at $\sqrt{s_{NN}}$ 2.76 TeV". In: *Physics Letters B* 754 (Mar. 2016), pp. 235–248. ISSN: 0370-2693. DOI: 10.1016/j.physletb.2016.01.020. URL: http://dx.doi.org/10.1016/j.physletb.2016.01.020.

[9] A. Adare et al. "Detailed measurement of the e^+e^- pair continuum in $p+p$ and $Au+Au$ collisions at $\sqrt{s_{\mathrm{NN}}}$ 200 GeV and implications for direct photon production". In: *Physical Review C* 81.3 (Mar. 2010). ISSN: 1089-490X. DOI: 10.1103/physrevc.81.034911. URL: http://dx.doi.org/10.1103/PhysRevC.81.034911.

[10] A. Adare et al. "Enhanced Production of Direct Photons in Au + Au Collisions at $\sqrt{s_{NN}} = 200$ GeV and Implications for the Initial Temperature". In: *Phys. Rev. Lett.* 104 (13 Mar. 2010), p. 132301. DOI: 10.1103/PhysRevLett.104.132301.

[11] S L Adler. "Photon splitting and photon dispersion in a strong magnetic field". In: *Annals of Physics* 67.2 (1971), pp. 599–647.

[12] S. L. Adler et al. "Photon Splitting in a Strong Magnetic Field". In: *Phys. Rev. Lett.* 25 (15 Oct. 1970), pp. 1061–1065. DOI: 10.1103/PhysRevLett.25.1061.

[13] G. S. Bali et al. "The QCD phase diagram for external magnetic fields". In: *Journal of High Energy Physics* 2012.2 (Feb. 2012). ISSN: 1029-8479. DOI: 10.1007/jhep02(2012)044.

[14] A. Bazavov et al. "The chiral and deconfinement aspects of the QCD transition". In: *Phys. Rev. D* 85 (2012), p. 054503. DOI: 10.1103/PhysRevD.85.054503. arXiv: 1111.1710 [hep-lat].

[15] Christian Bierlich et al. *A comprehensive guide to the physics and usage of PYTHIA 8.3.* 2022. arXiv: 2203.11601 [hep-ph]. URL: https://arxiv.org/abs/2203.11601.

[16] Christian Bierlich et al. "The Angantyr model for heavy-ion collisions in Pythia8". In: *Journal of High Energy Physics* 2018.10 (Oct. 2018). ISSN: 1029-8479. DOI: 10.1007/jhep10(2018)134. URL: http://dx.doi.org/10.1007/JHEP10(2018)134.

[17] J. D. Bjorken. "Energy Loss of Energetic Partons in Quark - Gluon Plasma: Possible Extinction of High p(t) Jets in Hadron - Hadron Collisions". In: (Aug. 1982).

[18] Szabocls Borsanyi et al. "Full result for the QCD equation of state with 2+1 flavors". In: *Phys. Lett. B* 730 (2014), pp. 99–104. DOI: 10.1016/j.physletb.2014.01.007. arXiv: 1309.5258 [hep-lat].

[19] P Buncic, M Krzewicki, and P Vande Vyvre. *Technical Design Report for the Upgrade of the Online-Offline Computing System.* Tech. rep. 2015. URL: https://cds.cern.ch/record/2011297.

[20] Adam Bzdak and Vladimir Skokov. "Event-by-event fluctuations of magnetic and electric fields in heavy ion collisions". In: *Physics Letters B* 710.1 (2012), pp. 171–174.

[21] Massimo D'Elia et al. "Phase diagram of QCD in a magnetic background". In: *Phys. Rev. D* 105 (3 Feb. 2022), p. 034511. DOI: 10.1103/PhysRevD.105.034511. URL: https://link.aps.org/doi/10.1103/PhysRevD.105.034511.

[22] Gabor David. "Direct real photons in relativistic heavy ion collisions". In: *Reports on Progress in Physics* 83.4 (Mar. 2020), p. 046301. ISSN: 1361-6633. DOI: 10.1088/1361-6633/ab6f57. URL: http://dx.doi.org/10.1088/1361-6633/ab6f57.

[23] Wei-Tian Deng and Xu-Guang Huang. "Event-by-event generation of electromagnetic fields in heavy-ion collisions". In: *Phys. Rev. C* 85 (4 Apr. 2012), p. 044907. DOI: 10.1103/PhysRevC.85.044907.

[24] B. Döbrich et al. "Magnetically amplified light-shining-through-walls via virtual minicharged particles". In: *Physical Review D* 87.2 (2013), p. 025022.

[25] Lyndon R Evans and Philip Bryant. "LHC Machine". In: *JINST* 3 (2008). This report is an abridged version of the LHC Design Report (CERN-2004-003), S08001. DOI: 10.1088/1748-0221/3/08/S08001. URL: https://cds.cern.ch/record/1129806.

[26] A. Fedotov et al. "Advances in QED with intense background fields". In: *Physics Reports* 1010 (2023). Advances in QED with intense background fields, pp. 1–138. ISSN: 0370-1573. DOI: https://doi.org/10.1016/j.physrep.2023.01.003.

[27] K. Fukushima. "Magnetic-field induced screening effect and collective excitations". In: *Physical Review D* 83.11 (2011), p. 111501.

[28] Kenji Fukushima, Dmitri E. Kharzeev, and Harmen J. Warringa. "Chiral magnetic effect". In: *Phys. Rev. D* 78 (7 Oct. 2008), p. 074033. DOI: 10.1103/PhysRevD.78.074033.

[29] Umut Gürsoy, Dmitri Kharzeev, and Krishna Rajagopal. "Magnetohydrodynamics, charged currents, and directed flow in heavy ion collisions". In: *Physical Review C* 89.5 (Feb. 29, 2024), p. 054905. ISSN: 0556-2813, 1089-490X. DOI: 10.1103/PhysRevC.89.054905.

[30] Umut Gürsoy et al. "Charge-dependent flow induced by magnetic and electric fields in heavy ion collisions". In: *Physical Review C* 98.5 (Aug. 23, 2023), p. 055201. ISSN: 2469-9985, 2469-9993. DOI: 10.1103/PhysRevC.98.055201.

[31] K. Hattori. "Birefringent photon spectrum from a nonlinear interaction with strong magnetic fiel". In: 2012.

[32] Koichi Hattori and Kazunori Itakura. "Vacuum birefringence in strong magnetic fields: (I) Photon polarization tensor with all the Landau levels". In: *Annals Phys.* 330 (2013), pp. 23–54. DOI: 10.1016/j.aop.2012.11.010. arXiv: 1209.2663 [hep-ph].

[33] Koichi Hattori, Kazunori Itakura, and Sho Ozaki. "Strong-field physics in QED and QCD: From fundamentals to applications". In: *Progress in Particle and Nuclear Physics* 133 (2023), p. 104068. ISSN: 0146-6410. DOI: https://doi.org/10.1016/j.ppnp.2023.104068.

[34] Koichi Hattori and Daisuke Satow. "Electrical conductivity of quark-gluon plasma in strong magnetic fields". In: *Physical Review D* 94.11 (Dec. 2016), p. 114032. ISSN: 2470-0010, 2470-0029. DOI: 10.1103/PhysRevD.94.114032. URL: https://link.aps.org/doi/10.1103/PhysRevD.94.114032 (visited on 01/24/2024).

[35] Werner Heisenberg and Hans von Euler. "Folgerungen aus der Diracschen Theorie des Positrons". In: *Zeitschrift für Physik* 98 (1936), pp. 714–732. URL: https://api.semanticscholar.org/CorpusID:120354480.

[36] Joey Huston, Klaus Rabbertz, and Giulia Zanderighi. *Quantum Chromodynamics*. 2023. arXiv: 2312.14015 [hep-ph]. URL: https://arxiv.org/abs/2312.14015.

[37] Gabriele Inghirami et al. "Magnetic fields in heavy ion collisions: flow and charge transport". In: *The European Physical Journal C* 80.3 (June 22, 2023), p. 293. ISSN: 1434-6044, 1434-6052. DOI: 10.1140/epjc/s10052-020-7847-4.

[38] Gabriele Inghirami et al. "Numerical magneto-hydrodynamics for relativistic nuclear collisions". In: *The European Physical Journal C* 76.12 (Oct. 30, 2023), p. 659. ISSN: 1434-6044, 1434-6052. DOI: 10.1140/epjc/s10052-016-4516-8.

[39] K. I. Ishikawa et al. "A numerical evaluation of vacuum polarization tensor in constant external magnetic fields". In: *International Journal of Modern Physics A* 28.20 (2013), p. 1350100.

[40] F. Karbstein et al. "Optical probes of the quantum vacuum: the photon polarization tensor in external fields". In: *International Journal of Modern Physics: Conference Series*. Vol. 14. World Scientific. 2012, pp. 403–415.

[41] F. Karsch. "Lattice results on QCD thermodynamics". In: *Nuclear Physics A* 698.1–4 (Feb. 2002), pp. 199–208. ISSN: 0375-9474. DOI: 10.1016/s0375-9474(01)01365-3. URL: http://dx.doi.org/10.1016/S0375-9474(01)01365-3.

[42] K. Kimura. "Numerical computation of virtual photon polarization due to ultra-intense magnetic field in the muon detector acceptance at ALICE". In: (2020). URL: https://www.quark.hiroshima-u.ac.jp/thesis/b202003_kimura.pdf.

[43] H. Koichi and I. Kazunori. "Vacuum birefringence in strong magnetic fields:(I) Photon polarization tensor with all the Landau levels". In: *Annals of Physics* 330 (2013), pp. 23–54.

[44] Norman M. Kroll and Walter Wada. "Internal Pair Production Associated with the Emission of High-Energy Gamma Rays". In: *Phys. Rev.* 98 (5 June 1955), pp. 1355–1359. DOI: 10.1103/PhysRev.98.1355.

[45] Wei Li, Shu Lin, and Jiajie Mei. "Conductivities of magnetic quark-gluon plasma at strong coupling". In: *Physical Review D* 98.11 (Dec. 2018). arXiv:1809.02178 [hep-ph, physics:hep-th, physics:nucl-th], p. 114014. ISSN: 2470-0010, 2470-0029. DOI: 10.1103/PhysRevD.98.114014. URL: http://arxiv.org/abs/1809.02178 (visited on 06/04/2024).

[46] Ewa Lopienska. "The CERN accelerator complex, layout in 2022. Complexe des accélérateurs du CERN en janvier 2022". In: (2022). General Photo. URL: https://cds.cern.ch/record/2800984.

[47] Michael L. Miller et al. "Glauber Modeling in High-Energy Nuclear Collisions". In: *Annual Review of Nuclear and Particle Science* 57.1 (Nov. 2007), pp. 205–243. ISSN: 1545-4134. DOI: 10.1146/annurev.nucl.57.090506.123020. URL: http://dx.doi.org/10.1146/annurev.nucl.57.090506.123020.

[48] Kouki Nakamura et al. "Relativistic resistive magneto-hydrodynamics code for high-energy heavy-ion collisions". In: *The European Physical Journal C* 83.3 (Mar. 2023). ISSN: 1434-6052. DOI: 10.1140/epjc/s10052-023-11343-y.

[49] Jajati K. Nayak and Bikash Sinha. "Electromagnetic signals from Au+Au collisions at RHIC energy, $\sqrt{s_{NN}} = 200$ GeV and Pb+Pb collisions at LHC energy, $\sqrt{s_{NN}} = 2.76$ TeV". In: *Physics Letters B* 719.1 – 3 (Feb. 2013), pp. 110–115. ISSN: 0370-2693. DOI: 10.1016/j.physletb.2012.12.057. URL: http://dx.doi.org/10.1016/j.physletb.2012.12.057.

[50] Tapan K. Nayak. "Probing the QCD phase structure using event-by-event fluctuations". In: *Journal of Physics: Conference Series* 1602.1 (July 2020), p. 012003. ISSN: 1742-6596. DOI: 10.1088/1742-6596/1602/1/012003. URL: http://dx.doi.org/10.1088/1742-6596/1602/1/012003.

[51] Jean-Fran çois Paquet et al. "Production of photons in relativistic heavy-ion collisions". In: *Phys. Rev. C* 93 (4 Apr. 2016), p. 044906. DOI: 10.1103/PhysRevC.93.044906.

[52] "Performance of the ALICE experiment at the CERN LHC". In: *International Journal of Modern Physics A* 29.24 (Sept. 2014), p. 1430044. ISSN: 1793-656X. DOI: 10.1142/s0217751x14300440. URL: http://dx.doi.org/10.1142/S0217751X14300440.

[53] Julian Schwinger. "On Gauge Invariance and Vacuum Polarization". In: *Phys. Rev.* 82 (5 June 1951), pp. 664–679. DOI: 10.1103/PhysRev.82.664.

[54] P. Skands, S. Carrazza, and J. Rojo. "Tuning PYTHIA 8.1: the Monash 2013 tune". In: *The European Physical Journal C* 74.8 (Aug. 2014). ISSN: 1434-6052. DOI: 10.1140/epjc/s10052-014-3024-y. URL: http://dx.doi.org/10.1140/epjc/s10052-014-3024-y.

[55] VV Skokov, A Yu Illarionov, and VD Toneev. "Estimate of the magnetic field strength in heavy-ion collisions". In: *International Journal of Modern Physics A* 24.31 (2009), pp. 5925–5932.

[56] Arturo Tauro. "ALICE Schematics". General Photo. 2017. URL: https://cds.cern.ch/record/2263642.

[57] S. K. Tiwari and C. P. Singh. "Particle Production in Ultrarelativistic Heavy-Ion Collisions: A Statistical-Thermal Model Review". In: *Advances in High Energy Physics* 2013 (2013), pp. 1–27. ISSN: 1687-7365. DOI: 10.1155/2013/805413. URL: http://dx.doi.org/10.1155/2013/805413.

[58] Kirill Tuchin. *Particle production in strong electromagnetic fields in relativistic heavy-ion collisions.* 2013. arXiv: 1301.0099 [hep-ph].

[59] Kirill Tuchin. "Time and space dependence of the electromagnetic field in relativistic heavy-ion collisions". In: *Phys. Rev. C* 88 (2 Aug. 2013), p. 024911. DOI: 10.1103/PhysRevC.88.024911.

[60] Simon Turbide, Ralf Rapp, and Charles Gale. "Hadronic production of thermal photons". In: *Phys. Rev. C* 69 (1 Jan. 2004), p. 014903. DOI: 10.1103/PhysRevC.69.014903. URL: https://link.aps.org/doi/10.1103/PhysRevC.69.014903.

[61] Vadim Voronyuk et al. "Electromagnetic field evolution in relativistic heavy-ion collisions". In: *Physical Review C—Nuclear Physics* 83.5 (2011), p. 054911.

[62] Yang Zhong et al. "A Systematic Study of Magnetic Field in Relativistic Heavy-Ion Collisions in the RHIC and LHC Energy Regions". In: *Advances in High Energy Physics* 2014.1 (2014), p. 193039.

[63] Yang Zhong et al. "Spatial distributions of magnetic field in the RHIC and LHC energy regions". In: *Chinese Physics C* 39.10 (2015), p. 104105.